Towards the impact of GMC collisions on the star formation rate

Glen H. Hunter [1,2,3]⋆ Paul C. Clark [3] Simon C. O. Glover [1] and Ralf S. Klessen [1,4]

[1]*Universität Heidelberg, Zentrum für Astronomie, Institut für Theoretische Astrophysik, Albert-Ueberle-Str 2, D-69120 Heidelberg, Germany*
[2]*SUPA, School of Physics & Astronomy, University of St Andrews, North Haugh, St Andrews KY16 9SS, UK*
[3]*School of Physics and Astronomy, Queen's Buildings, The Parade, Cardiff University, Cardiff CF24 3AA, UK*
[4]*Universität Heidelberg, Interdiszipläres Zentrum für Wissenschaftliches Rechnen, Im Neuenheimer Feld 205, D-69120 Heidelberg, Germany*

ABSTRACT

Collisions between giant molecular clouds (GMCs) are one of the pathways for massive star formation due to the high densities created. However, the enhancement of the star formation rate (SFR) is not well constrained. In this study, we perform a parameter study of cloud–cloud collisions and investigate how the resulting SFR depends on the details of set-up. Our parameter study explores variations in collision speed, magnetic field inclination (with respect to the collisional axis), and resolution, as defined by the number of cells per Jeans length. In all our collision simulations, we find a factor of 2–3 increase in the SFR compared to our no collision simulation, with star formation beginning sooner with (a) high collisional velocities, (b) parallel orientation between the magnetic field and collision axis, (c) and lower resolution. The mean virial parameter of high density (and thus possible star-forming) gas increases with collisional velocity, but has little variation with magnetic field inclination. The alignment of the velocity and magnetic field remains uniform in low-density environments but becomes more perpendicular with increasing density, indicating the compression of the magnetic field by collapsing gas. Comparing the trends in the SFR with other GMC collision studies, we find good agreement with studies that account for the gravitational boundedness of the gas in their star formation algorithm, but not with those that simply form stars above a prescribed density threshold. This suggests that the latter approach should be used with caution when modelling star formation on resolved cloud scales.

Key words: stars: formation – ISM: clouds – galaxies: ISM.

1 INTRODUCTION

Giant molecular clouds (GMCs) are large regions of gravitationally bound gas that exist within galaxies. These clouds typically span 1–100 pc in size and contain on the order $\sim 10^4$–10^6 $M_\odot$ of molecular gas, giving them typical hydrogen densities of ~ 100 cm^{-3} (Blitz 1993; Roman-Duval et al. 2010). GMCs have temperatures of ~ 10–30 K, a factor of 2–10 times lower than the temperature of the surrounding cold neutral medium. Due to their low temperatures and molecular nature, the main observational tracers of GMC properties are dust-continuum emission and molecular line emission (for e.g. CO/HCN/N$_2$H$^+$), which are used to observe GMCs within the Milky Way as well as in nearby galaxies (Fukui et al. 1999; Dame, Hartmann & Thaddeus 2001; André et al. 2010; Leroy et al. 2021).

Embedded within these GMCs are cooler dense clumps, the more massive of which are often observed as Infrared Dark Cloud. These clumps are accepted to be the precursor to star formation (Tan et al. 2014) due to their temperatures of 10–20 K (Chira et al. 2013) and higher number densities of $n_{H_2} = 10^4 - 10^6$ cm^{-3} (Motte, Bontemps & Louvet 2018). Each clump will likely form a cluster of stars due to further fragmentation and their relatively large-mass reservoir (10^2–10^5 $M_\odot$) (Motte et al. 2018). Despite many observations of these clumps, the process by which these clumps form is not fully understood. Some theoretical models have been proposed that explain how a GMC can fragment and further collapse, such as turbulence (Krumholz & McKee 2005), stellar and supernova feedback (Wareing, Pittard & Falle 2017), and converging gas flows, i.e collisions (Scoville, Sanders & Clemens 1986; Wu et al. 2017).

Numerical simulations of galactic discs have shown that GMC collisions are a recurring event due to the quasi-2D geometry of the distribution of dense molecular gas in most disc galaxies along with the differential rotation created by the gravitational potential of the galaxy (Tasker & Tan 2009). Estimates of the mean time between collisions range from $\sim$20 per cent (Dobbs, Pringle & Duarte-Cabral 2015) to $\sim$50 per cent (Sun et al., in preparation) of the orbital period of the clouds around the centre of the galaxy. Although this is a factor of a few longer than recent observational estimates of cloud lifetimes – between 10 and 30 Myr (Chevance et al. 2020) – it nevertheless implies that GMC collisions should be relatively common events. This is supported by the many observations of cloud collisions found within the Milky Way; for instance, Fukui et al. (2021) identify $\sim$50 GMCs that are candidates to be the product of cloud-cloud collisions (CCCs). However, collisions are not limited to the discs of galaxies. Cloud collisions have been observed in the small and large magellanic clouds (SMCs and LMCs) (Fukui et al. 2019; Tokuda et al. 2019; Neelamkodan et al. 2021) and theorized to occur with extreme collisional velocities in the centre of the Milky Way (Sormani et al. 2019). In the case of the SMC and LMC, these clouds collide as a result of large-scale H I flows caused by the tidal interactions of these satellite galaxies (Fukui et al. 2017). As for the centre of the galaxy, Sormani et al. (2019) argues the gas flow caused

⋆ E-mail: glen.hunter@uni-heidelberg.de

by the galactic bar crashes into the Central Molecular Zone, a ring of molecular gas surrounding the Milky Way nucleus, providing the ideal conditions for clouds to collide.

A variety of GMC collision simulations have been performed to explore various topics, such as observational signature of collisions (e.g. Haworth et al. 2015), triggering of high-mass star formation (e.g. Takahira, Tasker & Habe 2014; Balfour et al. 2015), and enhancement of the star formation rate (SFR), in both non-identical GMC collisions (e.g. Habe & Ohta 1992) and identical GMC collsions (e.g. Wu et al. 2017; Liow & Dobbs 2020; Tanvir & Dale 2020). Habe & Ohta (1992) and Takahira et al. (2014) show that the collision of a smaller cloud with a larger cloud creates a cavity and compression layer in which densities are reached that are high enough for high-mass stars to form. This is consistent with observations, for example of the Gum 11 cloud in the Carina Nebula Complex by Fujita et al. (2021), where CO observations indicate the presence of colliding clouds with a cavity, and with a massive star, HD92206, in close proximity to the compressed layer.

However, while there is general agreement that CCCs should enhance star formation, there is little agreement on *how much* the SFR is increased by a CCC. Recent simulations by Tanvir & Dale (2020) and Liow & Dobbs (2020) find that the SFR increases by a factor of two or less for collisions with relative velocities $v_{\rm rel} \leq 20\,{\rm km\,s^{-1}}$, typical of the majority of mergers that we expect to occur in a Milky Way-type spiral galaxy (Skarbinski, Jefferson & Goodman 2023). On the other hand, Wu et al. (2017) find an order-of-magnitude increase in the SFR for a collision with a relative velocity of $10\,{\rm km\,s^{-1}}$. The cause of the substantial discrepancy between the Wu et al. (2017) results and the results of the other cloud collision simulations is unclear, as the simulations differ in both their numerical approach[1] and their initial conditions. In particular, Wu et al. (2017) include a magnetic field in many of their simulations, while the other studies consider only the purely hydrodynamical case.[2] It is therefore not clear whether the difference in outcomes of these studies is a consequence of the different initial conditions adopted, or instead is a consequence of the choice of numerical approach.

In this paper, we attempt to improve our understanding of the effect of collisions on the SFR in magnetized clouds by performing a series of simulations of cloud collisions with different relative velocities and magnetic field orientations using a state-of-the-art MHD code – the AREPO moving-mesh code (Springel 2010) – and a sophisticated treatment of the microphysics of the gas (see Clark et al. 2019 and Appendix A) and the formation of stars (see Wollenberg et al. 2020 and Section 2.3). Importantly, for our fiducial case, we adopt the same initial conditions as in Wu et al. (2017, hereafter W17), allowing us to directly assess whether the large boost in the SFR that they find

---

[1]Liow & Dobbs (2020) and Tanvir & Dale (2020) use smoothed particle hydrodynamics (SPH) and model star formation with sink particles, while Wu et al. (2017) use an Eulerian grid code and model star formation with star particles. Both SPH studies adopt an isothermal equation of state, whereas Wu et al. (2017) employ a more realistic treatment of the heating and cooling that can occur during the collision, based on the microphysics of the interstellar medium.

[2]Other potentially important differences include the choice of initial cloud mass and relative velocity. Tanvir & Dale (2020) consider an initial relative velocity of $10\,{\rm km\,s^{-1}}$, as in W17, but simulate much smaller clouds, with masses of only $10^4\,{\rm M_\odot}$, compared to $\sim 10^5\,{\rm M_\odot}$ in W17. Liow & Dobbs (2020) carry out simulations for a wide range of cloud masses, including one that is within a few per cent of the W17 value, but only consider relative velocities $v_{\rm rel} \geq 20\,{\rm km\,s^{-1}}$, significantly higher than the case studied in W17.

in their study is due to their choice of initial conditions or to their numerical approach.

The structure of our paper as follows. In Section 2, we discuss the numerical approach taken, the initial conditions used for each simulation, and how the star formation is implemented. In Section 3, we present our results from the simulation, with a focus on the structure of the GMC, the SFR, and the virial parameter of the cloud. We conclude with a comparison of our results to other literature results in Section 4 and a summary of our findings in Section 5.

2 METHODOLOGY

2.1 Numerical magnetohydrodynamics

We make use of the AREPO moving mesh code to simulate the gas dynamics and star formation of colliding GMCs (Springel 2010). The code solves the equations of magnetohydrodynamics (MHD; Pakmor & Springel 2013),

$$\frac{\partial \rho}{\partial t} + \nabla \cdot (\rho \mathbf{v}) = 0\,, \tag{1}$$

$$\frac{\partial \rho \mathbf{v}}{\partial t} + \nabla \cdot (\rho \mathbf{v} \otimes \mathbf{v} + p_{\rm tot}\mathbf{1} + \mathbf{B} \otimes \mathbf{B}) = -\rho \nabla \Phi\,, \tag{2}$$

$$\frac{\partial \rho e}{\partial t} + \nabla \cdot [\mathbf{v}(\rho e + p_{\rm tot}) - \mathbf{B}(\mathbf{v} \cdot \mathbf{B})] = \dot{Q} + \rho \frac{\partial \Phi}{\partial t}\,, \tag{3}$$

$$\frac{\partial \mathbf{B}}{\partial t} + \nabla \cdot (\mathbf{B} \otimes \mathbf{v} - \mathbf{v} \otimes \mathbf{B}) = 0\,, \tag{4}$$

where ρ, $\mathbf{v}$, and $\mathbf{B}$ are the density, velocity, and magnetic field strength of a given cell, respectively. Here, $\mathbf{1}$ is the identity matrix. The total pressure is the sum of the thermal and magnetic pressures, $p_{\rm tot} = p_{\rm gas} + \frac{1}{2}|\mathbf{B}|^2$. The total energy per unit mass is $e = e_{\rm th} + \frac{1}{2}\mathbf{v}^2 + \Phi + \frac{1}{2\rho}|\mathbf{B}|^2$, where $e_{\rm th}$ is the thermal energy per unit mass. An adiabatic equation of state is adopted where $p_{\rm gas} = (\gamma - 1)\rho e_{\rm th}$ with $\gamma = 5/3$. Heating and cooling of the gas due to chemical changes and radiative processes is accounted for with the term $\dot{Q}$, which is discussed in more detail in Section 2.2.

The equations are solved on a tessellated Voronoi mesh in which the mesh-generating points are able to follow the gas flow using a Harten–Lax–van Leer discontinuity solver. This allows AREPO to act as a quasi-Lagrangian MHD code. The Voronoi mesh is adaptive: cells can be refined or de-refined by adding or removing mesh-generating points, respectively. The divergence-free constraint on the magnetic field, $\nabla \cdot \mathbf{B} = 0$, is enforced by the using the MHD solver provided in AREPO (Pakmor & Springel 2013). Here, additional source terms are added to equations (2–4), following the scheme introduced by Powell et al. (1999) combined with a hyperbolic Dedner cleaning (Dedner et al. 2002). This minimizes any effect that a diverging magnetic field may create.

The gravitational term is due to the self gravitation of the gas and any sink particles present within the system (see below). AREPO solves Poisson's equation,

$$\nabla^2 \Phi = 4\pi G \rho\,, \tag{5}$$

via a tree-based algorithm similar to the one used in the GADGET-2 code (Springel 2005), where G is the gravitational constant. The algorithm treats each cell as if the mass is at a point in the centre of the cell with a degree of gravity softening. The softening length for the gas is adaptive and is given as $\varepsilon_{\rm gas} = 2r_{\rm cell}$, where the $r_{\rm cell}$ is the radius of a sphere with the same volume as the Voronoi cell. The minimum softening length for both the gas and sink particles is 40.02 au. Further information on sink particles will be discussed in Section 2.3.

2.2 Chemical network

For our simulations, we make use of a modified version of the chemical network developed by Gong, Ostriker & Wolfire (2017), which itself is an improved version of prior networks developed by Nelson & Langer (1999) and Glover & Clark (2012). It includes a simplified treatment of the chemistry of H, C, and O and allows us to follow the evolution of the abundances of the main low-temperature gas coolants (CO, C, O, and C^+) with high accuracy, but low computational cost. A comprehensive description of the network can be found in Gong et al. (2017), and full details of the modifications we have made to it are described in Appendix A. Radiative heating and cooling of the gas are modelled using a detailed atomic and molecular cooling function, most recently described in Clark et al. (2019).

To treat the effects of H_2, C, and CO self-shielding, as well as shielding by dust, we make use of the TREECOL algorithm (Clark, Glover & Klessen 2012). It uses information stored in the gravitational tree structure to compute a 4π steradian map of the column densities of each of these species plus dust around each Voronoi cell. These maps are then used to determine how the interstellar radiation field (ISRF) reaching the cell is attenuated by self-shielding and dust absorption.

In all of our simulations, we adopt elemental carbon and oxygen abundances given by Sembach et al. (2000). Following Draine (1978), we set the strength of the ISRF to $G_0 = 1.7$ in Habing (1968) units. Finally, we adopt a value of $\zeta_H = 3 \times 10^{-17}$ s^{-1} for the cosmic ray ionization rate of atomic hydrogen.

2.3 Star formation

To simulate star formation, we make use of sink particles (henceforth sinks) to represent forming star clusters (Bate, Bonnell & Price 1995; Federrath et al. 2010). We follow the sink creation protocol outlined in Wollenberg et al. (2020). To summarize, the following conditions must be satisfied in order for a sink to be created:

a) The cell must have a density greater than a threshold density $\rho_c = 1.991 \times 10^{-16}$ g cm^{-3}. This threshold has been motivated by the work of Jones et al. (2021), who demonstrate that only collapsing – and thus actively star-forming – gas can reach such densities in such a set-up. Prole et al. (2022) show that, provided that the sink particles form within the collapsing regime, the SFR is insensitive to the exact choice of the threshold density. Note that while we could insert sink particles at lower densities, this reduces the efficiency of the algorithm, as it needs to check more candidates for sink creation. Also, this would increase the chance of converting gas to sinks, which while *currently* bound, may be subsequently disrupted via further interactions with the large-scale flows.

b) The gas flow within the accretion radius of the sink ($r_{acc} = 187$ au, corresponding to the Jeans length at the threshold density for a temperature of 10 K) must be converging. We ensure this by requiring convergence of both the velocity field ($\nabla \cdot \mathbf{v} < 0$) and the acceleration field ($\nabla \cdot \mathbf{a} < 0$).

c) The sink-forming region must be situated within a local minimum of the gravitational potential.

d) The cell must not lie within a distance $r < r_{acc}$ of an existing sink particle.

e) The region within r_{acc} must be gravitationally bound, i.e $|E_{grav}| > 2(E_{therm} + E_{kin})$ where E_{grav} is the gravitational energy, and E_{therm} and E_{kin} are the thermal and kinetic energies, respectively.
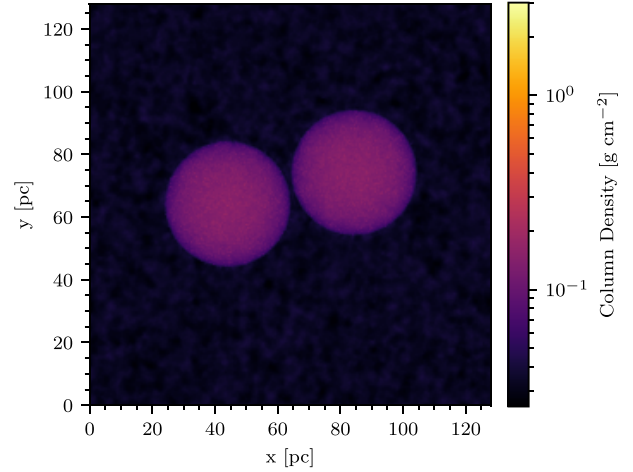
Figure 1. Surface density plot of the initial positions of the clouds.

If all of these criteria are met, the gas cell is converted into a sink that inherits its mass and momentum. This sink is able to interact gravitationally with the surrounding environment and is also able to accrete further gas onto itself. Any Voronoi cells with $\rho > \rho_c$ within a distance $r < r_{acc}$ of a sink are potentially eligible for accretion. However, gas is only accreted from the cell if it is gravitationally bound to the sink. Provided this is the case, enough gas is removed from the cell to reduce its density to ρ_c, although the total amount removed at each time-step is capped at 90 per cent of the cell's initial mass, for reasons of numerical stability. Following the accretion, any properties of the cell that depend on its mass are updated. It should be noted that the sinks formed do not contribute to the magnetic field of the system (i.e $|B_{sink}| = 0$). Given the size of our sink particles, and the density at which they are introduced, it is clear that they cannot be interpreted as individual stars, but rather as small-*N* protostellar systems. Also, given that there is no feedback from the young stars in our cloud, any star formation efficiencies reported in this paper should be considered as upper limits – our sink particles record the mass that is capable of going into stars (i.e. trapped in potential wells), in accordance with the above star formation model.

2.4 Initial conditions

In this paper, we adopt the initial conditions provided in W17, which were motivated by observations of GMCs. The simulations are initialized within a (128 pc)^3 domain of molecular gas with a mean molecular weight $\mu = 2.33$ and a helium-to-hydrogen fraction of 0.1. Two spherical clouds of radius $R_{GMC} = 20$ pc are placed into the domain with their centres separated by $(x, y, z) = (2R_{GMC}, b, 0)$ where $b = 0.5R_{GMC}$ (see Fig. 1). Each cloud is initialized with a mass of $M_{GMC} = 9.3 \times 10^4$ M$_\odot$ and an initial temperature of 15 K by randomly distributing 2 million mesh-generating points uniformly, which constructs our initial cells, achieving an initial mass resolution of 0.0465 M$_\odot$. This results in a hydrogen nucleon density of $n = 80.2$ cm^{-3} within the clouds where $n = \frac{\rho}{(1+4A_{He})m_p}$ with $A_{He} = 0.1$ being the helium-to-hydrogen fraction and m_p being the mass of a proton. Surrounding the clouds is a region of warmer molecular gas with $n = 7.14$ cm^{-3} and a temperature of T $= 150$ K. The clouds are not initially in thermal pressure equilibrium with the surrounding material. However, with an initial thermal to gravitational energy ratio of $E_{therm}/E_{grav} = 0.0066$, the clouds are significantly gravita-

Table 1. Initial conditions that are altered between simulations.

Simulation	θ ($°$)	$v_{\rm rel}$ (km s^{-1})	Cells per Jeans length
1	60	10	8
2	60	0	8
3	60	5	8
4	60	15	8
5	0	10	8
6	30	10	8
7	90	10	8
8	60	10	4
9	60	10	16

tionally bound against thermal pressure, and hence any loss of mass into the low-density surrounding medium is small.

A uniform magnetic field of $|B| = 10\,\mu$G in magnitude is set across the whole domain of the simulation. This results in an Alfvén velocity of $v_{\rm A} = 2.06$ km s^{-1} for each cloud and a mass-to-flux ratio that is six times greater than the critical value for both clouds (Glassgold & Langer 1974), making them magnetically supercritical. The angle θ is the magnetic field inclination from the x-axis in the x–y plane and is varied between simulations to investigate whether the orientation of the magnetic field affects the SFR (see Table 1).

We give the two clouds initial velocities of $v = +v_{\rm rel}/2$ and $v = -v_{\rm rel}/2$ for the clouds starting at negative and positive x, respectively, so that they will later collide at a relative velocity $v = v_{\rm rel}$. We carry out simulations with a range of different $v_{\rm rel}$, so that we can investigate how different collision strengths impact the SFR. We also include one case where $v_{\rm rel} = 0$ km s^{-1} (simulation 2) to allow us to investigate what happens in the absence of a collision.[3] Full details of the velocities used can be found in Table 1. Along with the collisional velocity, a turbulent velocity field is also applied to each cloud. The turbulence applied is purely solenoidal and has a 3D velocity dispersion of $\sigma = 3.46$ km s^{-1}. This follows a scaling law of $P(k) \propto k^{-4}$. For the velocity field within each cloud, the turbulence induced is both supersonic and super-Alfvénic, where $\mathcal{M} = \sigma/c_{\rm s} = 11.6$ and $\mathcal{M}_{\rm A} = \sigma/v_{\rm A} = 1.68$, respectively. The turbulence induced allows for each cloud to be in virial equilibrium, with the kinematic to gravitational energy ratio for each cloud being $E_{\rm kin}/E_{\rm grav} = 0.499$.

We also investigate the effect of varying the number of cells per local Jeans length (hereafter referred to as the Jeans refinement parameter, JR). To do this, we adopt Jeans refinement as our main cell refinement criterion in AREPO. Cells are refined by adding additional mesh-generating points whenever $D > \lambda_{\rm J}/$JR, where D is the effective diameter of the cell (i.e. the diameter of a sphere with the same volume as the mesh cell). We adopt JR = 8 as our default value for the Jeans parameter, but also investigate the behaviour of runs with JR = 4 and JR = 16, as detailed in Table 1.

We run the simulations as far as practical to establish a trend in the star formation history. The end time varies due to the adaptive time-step of the simulation, between 3 and 4 Myr. In the presence of close interacting objects, such as binaries, the time-step reduces significantly thus slowing the simulations progression.

3 RESULTS

3.1 Star formation rate

Each simulation results in a different star formation history. For an example, in Fig. 2, it can be seen that the systems evolve differently, creating unique structures. As a result, varying numbers of sink particles form in the simulations, as shown by the green dots in Fig. 2. To investigate this difference quantitatively, we look at the SFR of each of the simulations.

The SFR is calculated as:

$$\dot{M}_{\rm SFR} = \frac{\Delta M}{\Delta t} \tag{6}$$

where ΔM is the difference in the mass of the sinks between the start and end of a time-step of length Δt. These are calculated for each output snapshot available in all nine simulations. The results from these calculations are presented in Fig. 3 along with the total mass that has gone into star particles.

Fig. 3 shows that there is a clear difference in the time taken for stars to begin forming in the different runs, with a spread in onset times of $\sim$0.7 Myr between the most extreme cases. Looking in more detail at the results from the individual runs, we see that changing the collisional velocity has the greatest impact on the time required for star formation to begin. Stars start to form sooner in simulations with high collisional velocity than in simulations with low or zero collisional velocity. This behaviour is likely due both to the time it takes for large-scale shocks to form in the colliding clouds, and also to the density enhancement produced by these shocks. Faster collisions produce stronger shocks and hence larger density enhancements.[4] Therefore, higher density star-forming regions with shorter free-fall times are formed with increased collision velocity.

The orientation of the magnetic field has a smaller effect on the time required for star formation to begin. We see a clear difference in behaviour between the case with the magnetic field orientated parallel to the collisional axis, which forms stars after $\sim$1.5 Myr, and the runs with other magnetic field orientations, in which the onset of star formation is delayed by $\sim$0.25 Myr. The earlier star formation observed when the magnetic field is parallel to the collisional axis is a result of the magnetic field not hindering the compression of the gas along the x-axis. This allows the shocked gas to reach the densities required for the first sinks to be created more rapidly compared to the other magnetic field orientations (see also Appendix B). This delayed behaviour agrees well with that of the strong B_y simulation of Dobbs & Wurster (2021).

Finally, regarding the Jeans refinement variation, a higher resolution tends to delay the onset of star formation. This is likely due to the more highly resolved turbulent velocity field resulting in more disruption of the star-forming gas. This results in the gas being unable to be fully bound, delaying star formation. However, it should be noted that the difference of the onset of star formation between the $JR = 8$ and $JR = 16$ cases is small, of the order of $\sim$0.2 Myr, which is about the free-fall time of a dense core.

It is also informative to look at how the dense gas fraction – defined here as the fraction of the gas above a density of 10^4 cm^{-3} with

---

[3]Note that even in this case, the clouds will eventually collide due to their mutual gravitational attraction. However, this will occur on a time-scale >10 Myr, much longer than the period simulated here.

[4]Recall that for an isothermal shock, the strength of the density enhancement scales as the square of the Mach number. Although our model GMCs are not isothermal, the equilibrium temperature of the molecular gas varies only weakly with temperature, and so the isothermal result remains a useful guide.
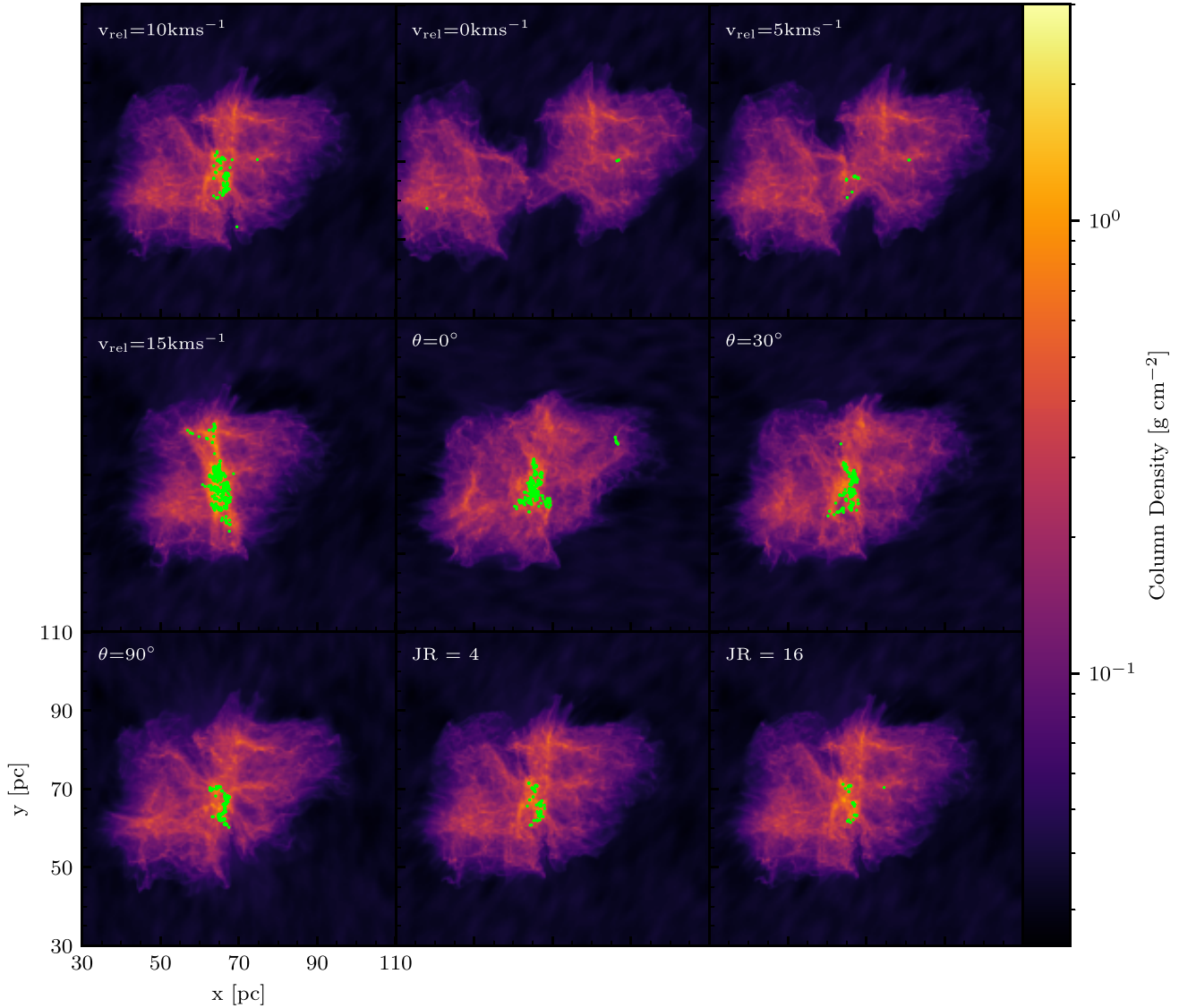
Figure 2. Column density plots of all simulations at $t = 2.40$ Myr. The green dots within the plot represent the sink particles that have formed.

common observational definitions (e.g. Lada, Lombardi & Alves 2010) – varies as a function of time in the different simulations. We illustrate this in the bottom three panels of Fig. 4 and as expected, dense gas is produced more rapidly as we increase the collision velocity, confirming our suspicion that the differences we observe in the timing of the onset of star formation are largely due to the differing amount of time it takes to compress the gas. Changing the orientation of the magnetic field also changes the dense gas fraction, with an appreciably higher fraction produced when the magnetic field is aligned with the axis of the collision. It is also apparent that there is an offset of around 0.5–1.0 Myr between the time taken to produce dense gas at 10^4 cm^{-3} and the onset of star formation. The offset reduces when we consider higher density gas fractions. This offset is easily understood as a consequence of our definition of 'dense' gas, and the fact that the density threshold for sink particle creation is significantly higher than the value we use in our definition of dense gas. At $n = 10^4$ cm^{-3}, the gravitational free-fall time of the gas is $\sim$0.5 Myr, and so we would expect gas close to this density to require around this long to collapse to stellar

densities (in reality) or the sink creation density (in the simulations).[5] The offset we see between the appearance of 'dense' gas and the formation of stars therefore corresponds to the one to two free-fall times required for gas at this density to collapse sufficiently to form stars.[6]

From Fig. 4, we observe significant variation of the gas fractions at early time-steps prior to the steady evolution of the gas density. Most of these variations are transient features in which denser gas forms

---

[5]Note that in a pure free-fall collapse, the time taken to collapse from 10^4 cm^{-3} to our sink creation density of $\sim$$10^8$ cm^{-3}, is two orders of magnitude longer than the time taken from collapse from $\sim$$10^8$ cm^{-3} to stellar densities.

[6]In the absence of pressure, we would expect the gas to collapse within a single free-fall time. In reality, however, the non-negligible magnetic pressure and kinematics of the gas inevitably delays the collapse (See Section 3.2). Finally, even once we account for this offset, it is clear that not all of the dense gas that forms in the simulations goes on to form stars. Instead, the star formation efficiency in gas of this density is typically only a few tens of per cent.
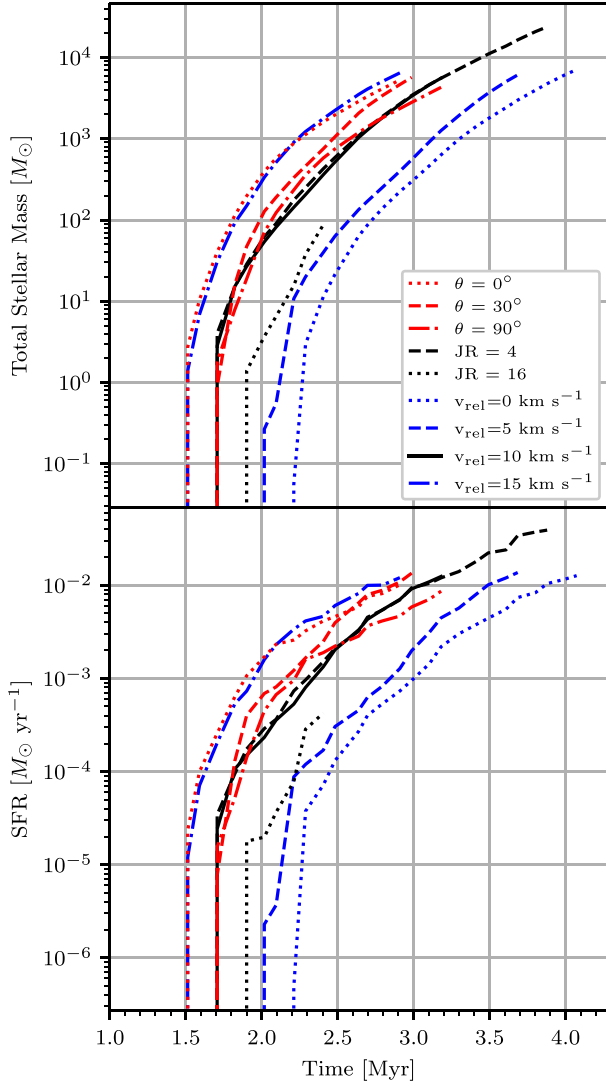
Figure 3. *Top*: Evolution of the mass in sink particles as a function of time in all nine simulations. *Bottom*: SFR as a function of time in all nine simulations.

due to the collision but is dispersed due to pressure gradients briefly forming. For the two lower density thresholds, we also see that there is a small fraction of gas above the threshold present at the beginning of the simulation. This results from the uneven distribution of mesh points within the initial conditions, which results in a certain amount of scatter in the starting densities of the cells.

The role of the collisions in driving the increase in the dense gas fraction and bringing about the onset of star formation can also be seen clearly if we examine how the dense gas fraction varies as a function of cloud separation, defined as the distance between the centres of mass of the two clouds. We see from Fig. 5 that most of the simulated clouds follow very similar tracks in this diagram, with substantial quantities of dense gas becoming apparent only once the cloud separation is less than ~25 pc, i.e. once the collision is significantly advanced. The two exceptions are the clouds with $v_{\rm rel} = 0$ and $5\,{\rm km\,s^{-1}}$, which start to develop dense gas while at clearly larger separations, particularly in the $v_{\rm rel} = 0\,{\rm km\,s^{-1}}$ run. These two runs are also the ones that produce the lowest dense gas fractions at any given time and that form the least number of stars. Our results are therefore consistent with the idea that in these runs, star formation is driven primarily by the collapse of the individual clouds, with the
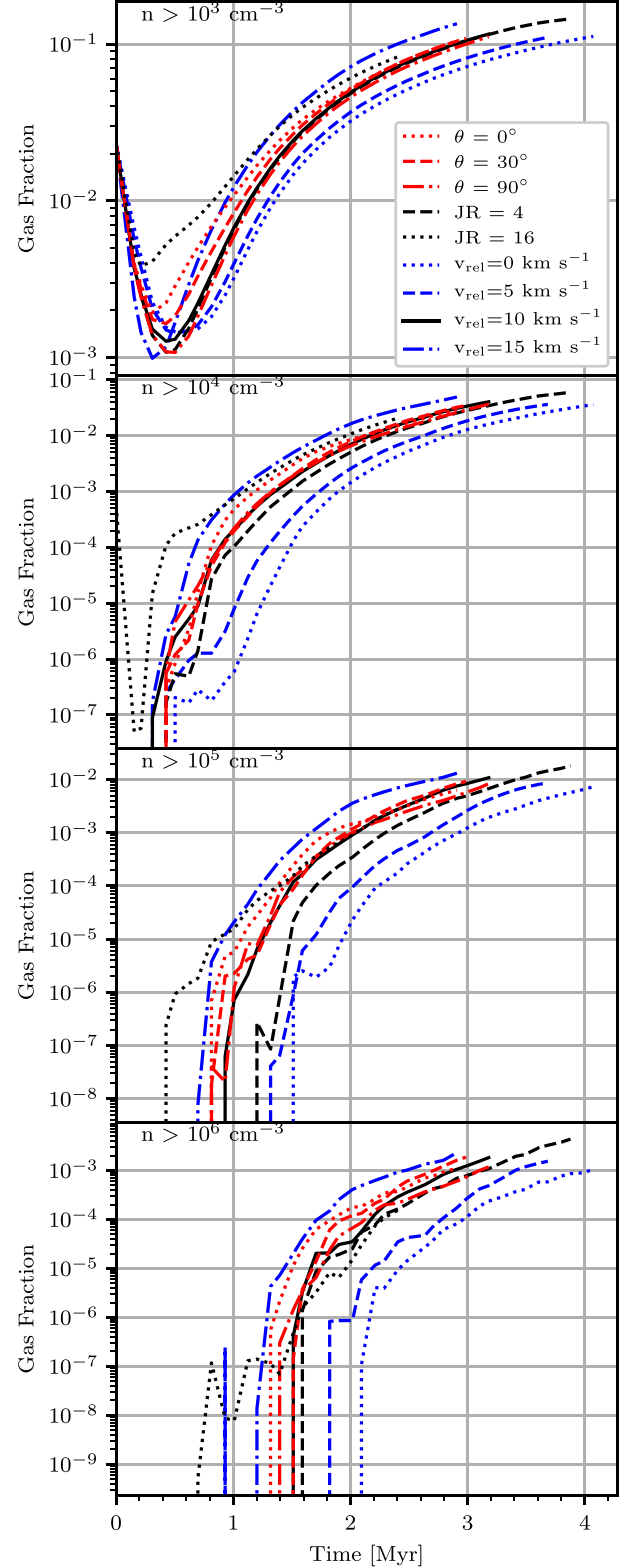

Figure 4. Fraction of gas above the specified density threshold in all nine simulations, plotted as a function of time. The thresholds are indicated in the top-left corner of each panel and are $n > 10^3\,{\rm cm^{-3}}$, $10^4\,{\rm cm^{-3}}$, $10^5\,{\rm cm^{-3}}$, and $10^6\,{\rm cm^{-3}}$ from *top* to *bottom*. We see that increasing the collisional velocity increases the amount of gas above the threshold for all values of the threshold, but that the effect is much stronger for the higher density thresholds.
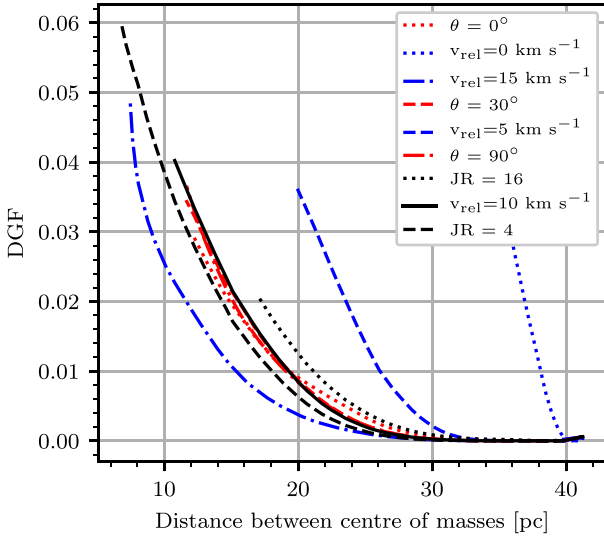
Figure 5. Fraction of dense ($n > 10^4\,\mathrm{cm}^{-3}$) gas in all nine simulations, plotted as a function of the separation between the clouds' centre of masses.

interaction between them playing little role, while in the simulations with higher v_{rel}, the collision between the clouds plays a much more substantial role in influencing the SFR.

Fig. 6 shows that the SFR in each simulation follows a similar trend from the point when sinks first form. For a brief period after the first sinks form, the SFR in the runs with $v_{\mathrm{rel}} > 0\,\mathrm{km\,s}^{-1}$ is as much as an order of magnitude larger than in the run with $v_{\mathrm{rel}} = 0\,\mathrm{km\,s}^{-1}$, in which the clouds do not collide. However, the difference between the runs quickly decreases, and for the majority of the time covered by our simulations, the SFR in the cloud collision runs is only a factor of 2–3 larger than in the zero velocity run. This behaviour agrees well with the enhancement in the SFR found by Liow & Dobbs (2020) and Tanvir & Dale (2020) for collision velocities below $20\,\mathrm{km\,s}^{-1}$. However, it is substantially smaller than the order of magnitude increase found by W17 despite the similarity between our initial conditions and theirs. To help us better understand the origin of this difference in results, we look in the next section at the virial parameter of the clouds and clumps formed in the simulations.

3.2 Impact on the virial parameter

In the previous section, we showed that although the cloud collision increases the SFR of our colliding clouds compared to the case with no collision, the magnitude of the increase is much smaller than the order of magnitude found by W17. This difference in outcome from their simulations cannot be a consequence of the initial conditions, as we use the same initial conditions as in their study, and hence must be a consequence of the difference in numerical approaches. As we discuss in more detail in Section 4, one of the main differences between our two studies is the algorithm we use to identify star-forming gas. W17 form stars stochastically in gas above a fixed density threshold, with no consideration given to whether or not the gas is gravitationally bound, whereas we use a sink particle-based approach in which stars form only in regions that are verifiably bound and collapsing. To understand whether this algorithmic difference can explain the difference in outcome, we explore how the virial parameter of the gas varies on different scales within our set of simulations.
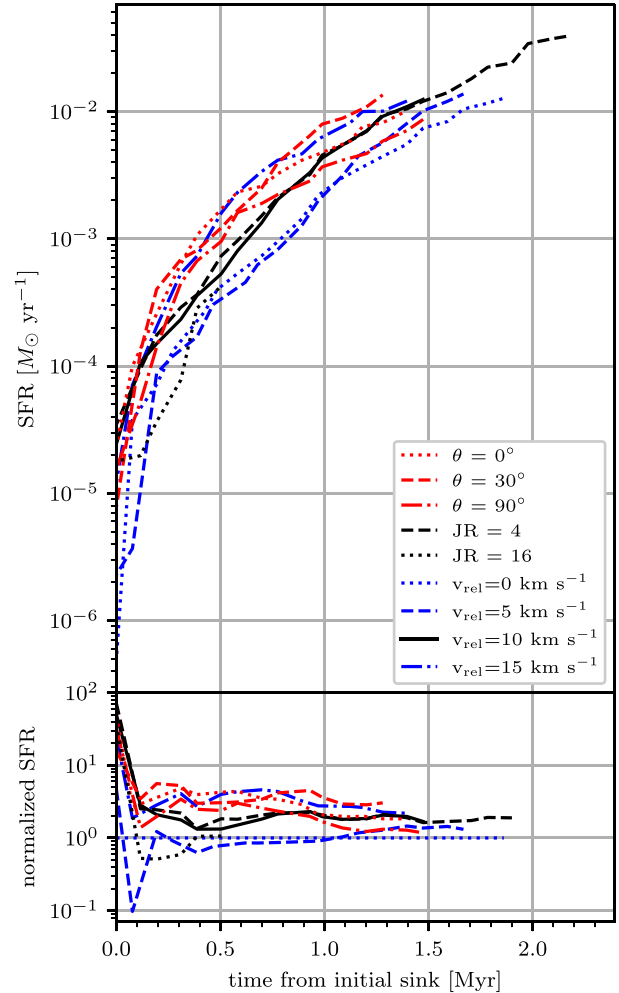

Figure 6. *Top*: SFR varying with time from initial sink formation for all simulations. *Bottom*: SFR normalized to $v_{\mathrm{rel}} = 0\,\mathrm{km\,s}^{-1}$ SFR as a function of time from initial sink formation.

The virial parameter η provides an insight into how bound the star-forming region is by comparing the gravitational energy against all other energy contributions. We adapt the definition provided in Bertelli Motta et al. (2016) to include magnetic energy as a factor which counteracts gravitational collapse (equation 7).

$$\eta = \frac{2(E_{\mathrm{kin}} + E_{\mathrm{therm}} + E_{\mathrm{mag}})}{|E_{\mathrm{grav}}|} \qquad (7)$$

We chose to include the magnetic energy in this calculation as the gas we are considering has a density below the sink formation threshold and does not exist near sinks. It should be noted that the magnetic energy is not accounted for in the energy check of the sink creation protocol.[7]

In order to make the comparison between the simulations, we perform this analysis on the snapshots that are ~ 1 Myr after the formation of the first sink particle in each simulation. Note that this corresponds to a different physical time in each simulation, but

---

[7]In cases where the magnetic energy is high enough in the sink formation region to prevent collapse, we would also expect it to halt the infall of the gas, i.e. independent of the energy check, the region will fail condition (b) of the sink creation protocol and hence will not be converted into a sink.

should allow us to compare the clouds when they are at a similar stage in their evolution.

The regions used to determine the virial ratio are chosen by using the local minima of the potential. These are identified as part of the flux calculations within the MHD code and are stored within the outputs. After identification, we then compute the Jeans length for the gas located at the potential minimum. For the purposes of this analysis, we want to avoid potential minima that have already formed stars, so that we can measure the virial ratio accurately without worrying about the confounding effect of the sink particles.[8] We therefore remove from consideration any minima that are located within two Jeans lengths of a sink particle. We next select all gas cells lying within a single Jeans length of the identified minimum and compute the total gravitational, kinetic, magnetic, and thermal energies of this set of gas cells. The gravitational energy, E_{grav}, is calculated via a direct N-body approach,

$$E_{grav} = -\sum_{i=1}^{N} \sum_{j=i+1}^{N} \frac{Gm_i m_j}{\Delta r_{ij}} \quad (8)$$

where m_i and m_j are the masses of the ith and jth cells, respectively, Δr_{ij} is the separation between the cells, and N is the total number of cells within the selected region. The kinetic, magnetic, and thermal energies, E_{kin}, E_{mag}, and E_{therm}, are calculated as follows:

$$E_{kin} = \frac{1}{2} \sum_{i=1}^{N} m_i v_i^2 \,, \quad (9)$$

$$E_{mag} = \frac{1}{8\pi} \sum_{i} |B_i|^2 \Delta V_i \,, \quad (10)$$

$$E_{therm} = \sum_{i} m_i e_{th_i} \,, \quad (11)$$

where m_i is the mass of cell i, v_i is the velocity of the cell relative to the potential minimum considered, $|B_i|$ is the magnetic field strength of the cell, $\Delta V_i = m_i/\rho_i$ is the approximate cell volume where ρ_i is the cell density, and e_{th_i} is the thermal energy per unit mass of the cell.

The number densities associated with the local minima of the potential cover a wide range of values. For the purpose of this analysis, we focus on a range of associated hydrogen nuclei number densities from $n = 100$ cm^{-3} to 10^6 cm^{-3}. Our motivation for adopting a lower limit of 100 cm^{-3} is to ensure that are selecting regions associated with the cloud and not the surrounding intercloud medium. The upper limit is chosen to match the density threshold for star formation used in W17. We split the data into four bins of 1 dex in density starting at 10^2–10^3 cm^{-3}.

In Fig. 7, we show the ratio of each of the different components of the energy (thermal, magnetic, and kinetic) to the gravitational energy, as well as the averaged virial parameter, for the hydrogen nuclei number density n bin considered for varying collisional velocity. The error bars indicate the full range of values of each parameter in each bin, i.e. the range from the minimum to the maximum value of the parameter.

Upon first inspection, we note that the virial parameter is considerably greater than 1 in almost all of the regions we consider. This would imply that they are not gravitationally bound and thus unable to form stars at this point as a result. While this is likely true for some regions, particularly in our lower density bins, it should also be noted

Figure 7. From the top down: The average (a) thermal-to-gravitational-energy ratio, (b) magnetic-to-gravitational-energy ratio, (c) kinetic-to-gravitational-energy ratio, and (d) virial parameter for different collisional velocities v_{rel} at 1 Myr after first sink formation. The error bars indicate the full range of values obtained. Each density bin is indicated with the corresponding bracket annotation with the separation of the points for ease of reading. The points within a bracket are for the same density bin but are offset in the figure for clarity.

that we are considering only a single Jeans length from the potential minimum, and therefore we would expect to recover $\eta \sim 1$ for this region even if the kinetic and magnetic energies were zero.[9] Since

---

[8]As sink particles selectively remove the most bound gas, the virial ratio in the remaining gas will inevitably be higher than it would be in the same region if the sink were not present.
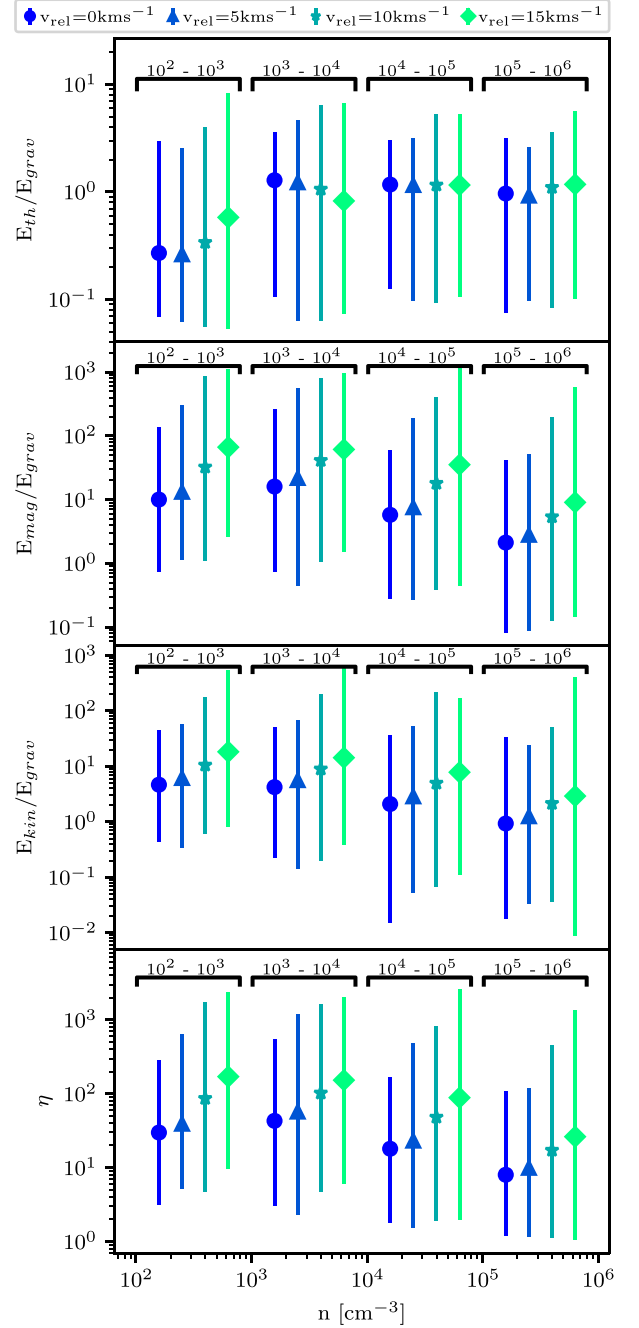
[9]We do not recover exactly one because the density and temperature are not constant within the selected region.

these components are not zero, it is unsurprising that we recover $\eta \gg$ 1 for most of these regions, even the ones that will later form stars. In practice, all that this means is that the radius of the region that will ultimately collapse is greater than a single Jeans length, owing to the additional support provided by the turbulent motions and the magnetic field. Nevertheless, this does provide a clear demonstration of the difficulties involved in identifying star-forming regions based on the properties of individual gas cells, as is the case when applying, for example, a simple density threshold, since ultimately the answer to the question of whether or not this gas will collapse and form stars depends not only on its own properties but also those of the surrounding gas cells.

For the purposes of the comparison we are making here, we look for differences in the parameters between the simulations considered, and in particular for any general trends. For the ratio of E_{therm} to E_{grav}, we do not see a clear trend with collision velocity: the ratio increases with increasing v_{rel} in some density bins, but decreases or remains constant in other density bins. However, we observe a consistent increase in the ratios of E_{mag} to E_{grav} and E_{kin} to E_{grav} with increasing v_{rel} in all density bins. This is then reflected in the behaviour of the virial parameter, which also increases with increasing v_{rel} at all densities. This behaviour is a consequence of an increase in the turbulent motion of the dense molecular gas as the clouds collide with higher velocities. This directly increases the kinetic energy, but also results in additional tangling of the magnetic field, which increases the magnetic field strength and magnetic energy. These motions generally act against gravitational collapse and as a result fewer regions become gravitationally bound and star-forming, leading to a smaller increase in SFR than anticipated by W17.

We have repeated the same analysis for the simulations with differing initial magnetic field inclinations (Fig. 8). Once again, we find that the ratio of E_{therm} to E_{grav} is substantially less than one in our lowest density bin and of order unity in the other bins. In the lowest density bin, we also observe a decrease in the average value of this ratio with increasing inclination angle. A reason for this could be that the gravitational energy calculated for these densities in the $\theta = 0°$ simulation is higher due to compactness. The regions considered for this density bin exist on the outer parts of the clouds and visual inspection of the density maps shows more 'flaring' at the edges for greater magnetic field inclinations than for $\theta = 0°$ (see also Figs B1 and B2). We see no clear trend in the value of the ratio with magnetic field inclination angle in the other density bins. As for the magnetic and kinetic to gravitational energy ratios, we find the values of these ratios to be similar across the different inclinations within a given density bin. This in turn results in the virial ratio being constant across all magnetic field orientations for each density bin.

3.3 Flow alignment to magnetic field

The movement of gas within a magnetic field causes that field to be dragged, distorting the magnetic field in the process. The compression of the field lines causes the flow of gas to slow down as the magnetic field resists the flow. However, this only applies if the direction of flow is not parallel to the magnetic field. The flow remains unhindered if it is parallel to the magnetic field. Examining the alignment between the flow and the magnetic field can therefore tell us something about the degree to which the field is influencing the motion of the gas.

For this purpose, we define the alignment as the dot product of the velocity and magnetic fields normalized by the magnitude of the
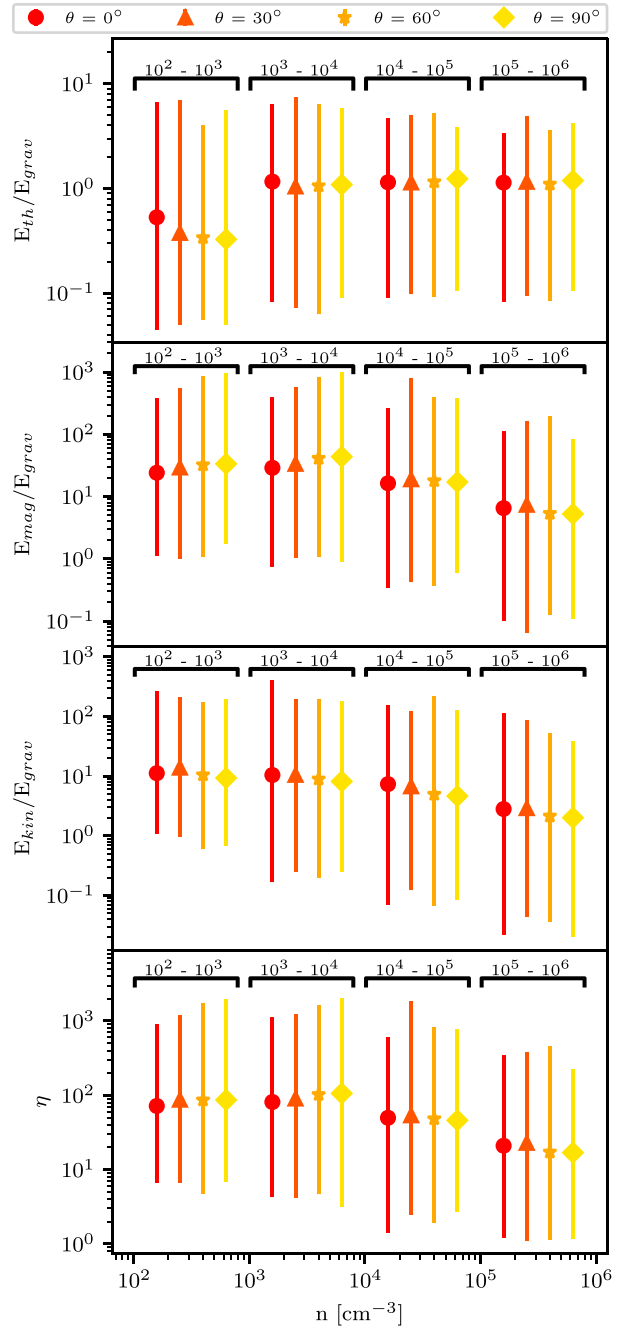

Figure 8. Same as Fig. 7 but looking at the differences in the inclination of magnetic field.

fields, in other words:

$$\text{Alignment} = \frac{\mathbf{v} \cdot \mathbf{B}}{|\mathbf{v}||\mathbf{B}|} \qquad (12)$$

This yields the cosine of the angle between the magnetic field and the flow velocity for each Voronoi cell, which has values ranging from -1 to 1, with the extremes meaning the fields are parallel whilst a value of 0 means the fields are perpendicular. This corresponds to unrestricted and fully restricted flow by the magnetic fields, respectively. In Figs 9 and 10, we explore how the field alignment varies between our four density bins in runs with different relative velocities and magnetic field inclinations. In each case, the count of the points at each alignment is normalized by the total number
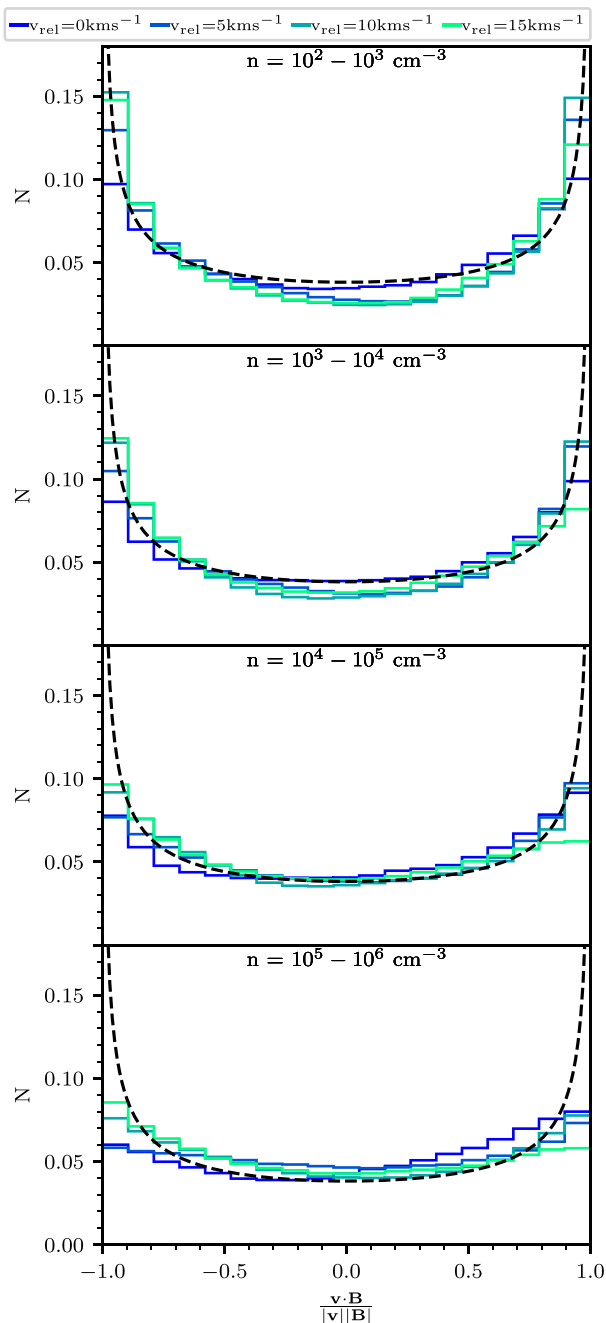
Figure 9. Weighted histogram of the velocity and magnetic field alignment for differing collisional velocities at 1 Myr after first sink formation. Each subplot represents a different density bin. The black dashed line represents the distribution we would expect if the alignment is random.

Figure 10. Same as Fig. 9 but for varying magnetic field inclination.

of points within the relevant density bin. The analysis is carried out using the same snapshots, as in Section 3.2.

In low-density regions (10^2–10^4 cm^{-3}), we find a distribution of alignments similar to what we would expect for a fully random distribution (indicated in Figs 9 and 10 by the black dashed line). In the highest collision velocity runs ($v_{rel} \geq 10$ km s^{-1}), there is a slight skew in the distribution of alignments that we have traced to a similar skewness in the distribution of alignments in the initial conditions (See Fig. 11). Similarly, in the runs with $\theta = 0°$ and $\theta = 90°$, we also see a clear imprint of the initial conditions, with a preference for parallel alignments in the run with $\theta = 0°$ and for perpendicular
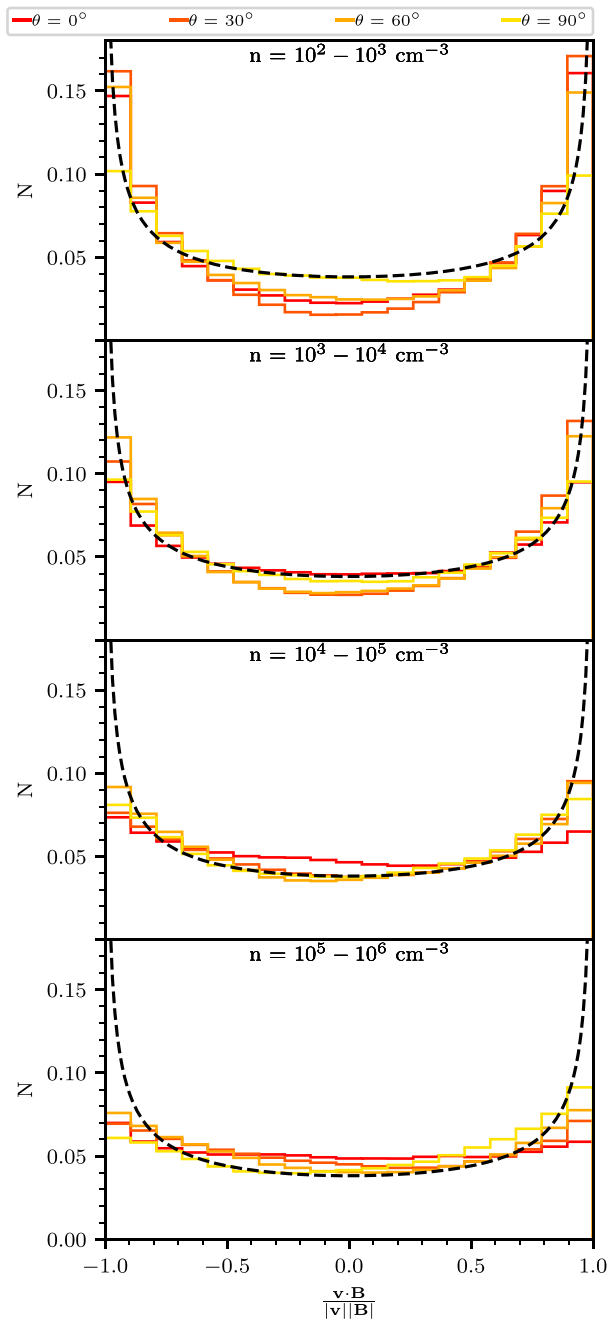
alignments in the run with $\theta = 90°$. Overall, there is little indication that the field plays a significant dynamical role in the low-density gas.

At higher gas densities (10^4 – 10^6 cm^{-3}), we no longer see any clear imprint of the initial conditions. The distribution of alignments close to 0.0 becomes very similar to what we would expect for a fully random distribution. However, there is a clear deficit of alignments close to -1 and $+1$ that becomes more pronounced as the density increases. In other words, in dense gas, the gas flow is pre-dominantly perpendicular to the field, rather than parallel to it. This behaviour is consistent with our expectations for magnetically supercritical gas: the flow of gas perpendicular to the magnetic field compresses and strengthens the field, while the flow of gas along the field lines leaves the field strength unaltered, resulting in a field alignment that
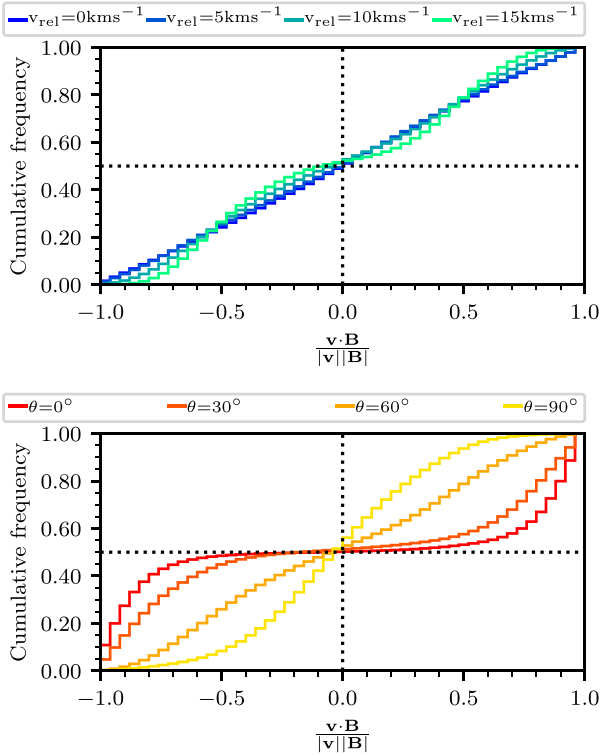
Figure 11. Cumulative distribution of the initial alignment of the simulations at $t = 0$ Myr. *Top*: Varying collisional velocity. *Bottom*: Varying magnetic field inclination. The dashed black lines represent where the cumulative distribution would encompass 50 per cent of the data assuming a Gaussian distribution of alignments. Points in the top-left and bottom-right quadrants are indicative of a skewed distribution.

becomes increasingly perpendicular as the compression continues. This behaviour has been seen in other simulations (such as Soler & Hennebelle 2017) and is a result of velocity field convergence, $\nabla \cdot v < 0$ (Boldyrev 2006; Matthaeus et al. 2008).

One further important take away from these results is that in the densest gas, there are only minor differences in the field alignment between the different runs, consistent with a picture in which the small-scale behaviour of the field in dense regions is primarily determined by the local velocity field and not by the large-scale details of the collision.

4 DISCUSSION

4.1 Comparison with W17

Our simulations demonstrate that rapid collisions between clouds lead to an earlier onset of star formation than in clouds that collide slowly or not at all. However, the way in which star formation proceeds once the process has set in is remarkably similar in all of our simulations. Note we find a persistent enhancement of a factor of 2–3 in the SFR in our colliding clouds compared to our $v_{\text{rel}} = 0$ km s^{-1} control run. The earlier onset of star formation and the increase in the SFR due to the collision are similar to the results reported by W17 for the same initial conditions. Contrary to W17, we find a only a very weak dependence of the SFR on the collisional velocity, v_{rel}.

It is worthwhile considering possible methodological reasons for this difference. Aside from our use of a different magnetohydrody-

namical code (Wu et al. use ENZO, we use AREPO), our simulations differ from those of W17 in two main respects: our star formation algorithm and our treatment of chemistry and cooling.

4.1.1 Star formation protocol

In our simulations, we make use of sink particles as our representation of stars/protostellar systems, which are able to continue accreting after forming (see Section 2.3). In contrast, W17 make use of star particles that are formed stochastically with a fixed efficiency per free-fall time in gas cells on the finest level of refinement in their simulation that satisfy a suitably chosen criterion. In their 'density-regulated' models, this criterion is a simple density threshold: star formation is permitted only in gas denser than $n_{\text{th}} = 10^6$ cm^{-3}. In their 'magnetically regulated' models, on the other hand, star formation is permitted only in cells that are magnetically supercritical, although their adoption of a fixed star particle mass also acts as an effective density threshold, preventing stars from forming in cells less dense than 3.55×10^5 cm^{-3} in most of their 'magnetically regulated' runs. Notably, W17 do not require the gas flow to be converging or the gas to be gravitationally bound in order for it to be eligible to form stars.

A final difference between the treatment of star formation in the two approaches is that the star particles formed in the W17 simulations have a fixed mass from the moment that they form, whereas our sink particles can continue to accrete mass as they age. W17 argue that fixing the star particle mass is a way of approximately accounting for the effects of stellar feedback, but a comparison between our runs and those of W17 shows that we actually recover much lower SFRs, by around an order of magnitude, even without this restriction. Similar to the studies by W17, we also do not take stellar feedback into account in this set of simulations. Neglecting supernovae is justified because our computation covers a period of only a few Myr after the onset of star formation (see Fig. 6), which is shorter than the time required for the first supernovae to occur (Kippenhahn, Weigert & Weiss 2013). Ignoring stellar winds and radiation is also justified at early times, but is less valid once the total stellar mass exceeds a few hundred solar masses, as at this point we would expect to have formed at least a few stars massive enough to start ionizing their surroundings and driving strong stellar winds. Nevertheless, the importance of these forms of feedback for gas removal depends very much on the properties of the star cluster and its parental cloud (e.g. Rahner et al. 2017; Haid et al. 2018; Rahner et al. 2019), and it is unclear how much impact they would have in our simulated clouds.

We also note that our main results do not depend on this simplification. The difference between the SFRs in the different runs becomes apparent very early on, long before stellar feedback from massive stars could possibly play a role in the evolution of the clouds, and so even if we were to have terminated our simulations at the point that the first massive star forms in each case, we would have come to the same conclusions. Finally, the neglect of feedback from protostellar outflows likely does affect the SFR at all times in the simulation. However, previous numerical studies have shown that the impact of this form of feedback is always negative: it reduces the SFR by a factor of around 2–3 compared to models that do not account for it (see e.g. Federrath 2015; Hu et al. 2022). Its absence from our simulations therefore cannot explain the discrepancy between our results and those of W17.

We have assumed that the impact of stellar feedback on the SFR is always negative. This is a good approximation on the scales of individual star-forming clouds (Grisdale et al. 2017), but on larger

scales it is possible that feedback could in some circumstances be positive, triggering the compression of gas and the onset of star formation somewhere else in the galaxy (Shore 1981). However, exploring the effect of feedback on these scales lies far outside of the scope of this paper.

The simplest explanation for the difference between our study and the results of W17 is the different star formation criteria applied in the two approaches. W17 motivate their adoption of a simple density or mass-to-flux ratio threshold on the grounds of the limited resolution of their simulations (smallest cell size $\Delta x = 0.125$ pc), which does not make them confident that they can resolve the small-scale structure of the gas well enough to apply a more complicated criterion. Our spatial resolution is much better in gravitationally collapsing regions, thanks to the Jeans refinement criterion, with our minimum cell size becoming as small as $\sim 10^{-4}$ pc shortly before sink particle formation. We therefore do a much better job of resolving the structure of the dense gas and can easily distinguish between dense gas that is gravitationally bound and star-forming and dense gas that is not gravitationally bound. Since there is evidence that a significant fraction of the dense gas produced in the collisions is not gravitationally bound, as we have already seen in Section 3.2, it is therefore unsurprising that we recover much smaller SFRs than in the W17 simulations, but that are much more in line with the results found by other studies using a sink particle based approach (Tanvir & Dale 2020; Dobbs, Liow & Rieder 2020).

The sink particle studies mentioned here do differ in their sink protocols. All studies include a sink creation density threshold and require the sink-forming cell (or particle) to lie at a potential minimum. Whilst this study and Liow & Dobbs (2020) have a similar protocol (this study having a higher sink creation density threshold), Tanvir & Dale (2020) do not have either a gas convergence or a boundedness check in their sink creation protocol. Instead, they opt for further constraints on where sinks form that required that the sink-forming gas is not tidally interacting with other sinks, and that it is capable of undergoing free-fall collapse before interacting with another sink.

The lower density threshold of Liow & Dobbs (2020) could conceivably result in more sink particles forming than in our simulation, but the factor by which the SFR is enhanced should be unaffected provided the threshold density is consistent in simulations with and without collision. The same argument can be made for Tanvir & Dale (2020): we would again expect their comparison of SFRs between colliding and non-colliding runs to be meaningful, since their protocol is consistent across the simulations.

The differences in the sink creation protocol has scope to yield significant differences in the SFR enhancement across the studies, yet it has not. This suggests that the active accretion onto sink particles limits the enhancement in the SFR with GMC collisions in comparison to fixed mass star particles.

That all said, we stress that this remains merely our most plausible hypothesis for the difference in outcomes. To confirm, this would require us to carry out simulations similar to the ones presented here but using exactly the same star formation prescription as in W17, as well as simulations with the same initial conditions as Tanvir & Dale (2020) and Liow & Dobbs (2020), a task which is outside of the scope of our current study.

It should also be noted that the use of star particles in the context of molecular cloud/GMC-scale star formation is uncommon. Previous works looking at colliding clouds or flows mostly use a sink particle based prescription for star formation (for example Tanvir & Dale 2020; Dobbs et al. 2020; Dobbs & Wurster 2021). A star particle approach is more commonly used in galaxy-scale and
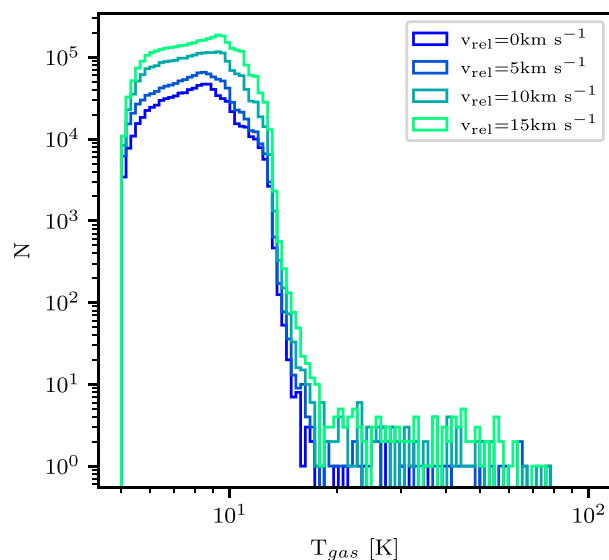

Figure 12. Temperature distribution of all gas cells of $n \geq 10^5 \text{cm}^{-3}$ for different collisional velocities at 1 Myr after initial sink particle creation.

larger simulations where individual GMCs are at best barely resolved. On these scales the justification for a probabilistic approach to star formation is acceptable as the gravitationally bound cores within GMCs are not resolved and the GMCs themselves are not necessarily gravitationally bound (e.g. see Dobbs, Burkert & Pringle 2011).

4.1.2 Treatment of chemistry and cooling

Although we consider the difference in the star formation algorithm to be the most likely cause of the difference between our results and those of W17, it is worthwhile examining whether the difference in our chemical and thermal treatment may also play a role here. As previously mentioned, in our simulations, we use a modified version of the Gong et al. (2017) chemical network, together with the atomic and molecular cooling function described in Clark et al. (2019). On the other hand, W17 make use of the GRACKLE library (Smith et al. 2017). The chemical networks provided in GRACKLE allow one to model the non-equilibrium chemistry of hydrogen (including H_2 formation and destruction), but do not account for the chemistry of metals such as carbon or oxygen. To account for heating and cooling due to metals, GRACKLE uses a table-based approach: the relevant rates are interpolated from a set of tables in which the rates are given as a function of density, temperature, and (optionally) metallicity. GRACKLE includes several sets of tables computed using the CLOUDY photodissociation region (PDR) code (Ferland et al. 1998), but also allows the user to supply their own. W17 make use of this latter option, using a set of cooling tables generated by Wu et al. (2015) using the PyPDR code (Bruderer 2019).

The impact of this difference in approach can be seen if we compare the temperature distribution of the dense gas in our simulations (shown in Fig. 12) with the temperature distribution of the star-forming gas in the W17 simulations (shown in their fig. 6). We find that most of the dense gas in our simulations has a temperature in the range $5 < T < 20$ K, with a small tail in the distribution extending up to ~ 100 K. We also find that there is no clear difference in the temperature distribution of the dense gas between the colliding ($v_{rel} > 0 \text{ km s}^{-1}$) and the stationary ($v_{rel} = 0 \text{ km s}^{-1}$) clouds. On the other hand, W17 recover a somewhat broader temperature distribution, covering the range $10 < T < 40$ K in their non-colliding runs
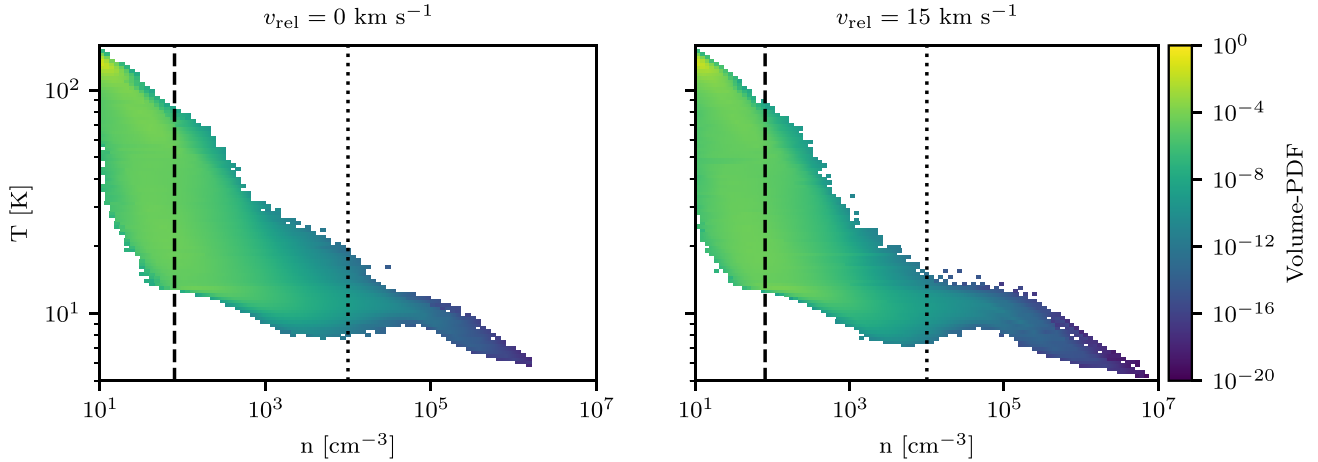
Figure 13. Volume-weighted temperature-density phase diagram for $v_{\rm rel} = 0\,{\rm km\,s^{-1}}$ (left-hand panel) and $v_{\rm rel} = 15\,{\rm km\,s^{-1}}$ (right-hand panel), shown for the snapshot immediately prior to the formation of the first sink particle. The dashed vertical line is the initial density of the clouds and the dotted vertical line is the density above which we consider the gas to be dense. The impact of $v_{\rm rel}$ on the temperature distribution is small, owing to the short cooling time of the gas.

and extending up to ∼100 K in the colliding runs. This broader temperature distribution may be a consequence of the stronger UV field adopted in their calculation – they assume $G_0 = 4$, compared to $G_0 = 1.7$ here – or may be due to some other aspect of the way in which cooling is treated in the two sets of simulations. Whatever the reason, it is clear that the difference in temperature distributions cannot explain the different SFRs recovered in the simulations: the dense gas in our simulations is colder on average than that that in the W17 models and hence has less thermal support, meaning that it should be more likely to form dense regions and then stars, rather than less likely. Fig. 13 demonstrates this point by showing the temperature-density distribution of the gas in the simulations with $v_{\rm rel} = 0\,{\rm km\,s^{-1}}$ and $v_{\rm rel} = 15\,{\rm km\,s^{-1}}$ at the snapshot just before sink formation. We see that the phase diagram is similar in both simulations, although there is more dense gas in the run with $v_{\rm rel} = 15\,{\rm km\,s^{-1}}$. If the difference between the simulations were due solely to the difference in the temperature distributions, we would expect to find a higher SFR in our simulations than in W17, which is the opposite of what we actually see.

4.2 Do cloud collisions trigger star formation?

There is growing observational evidence, summarized recently by Fukui et al. (2021), that the formation of massive stars is often associated with molecular clouds that show signs of having undergone a CCC. This suggests that collisions are generally the cause of the formation of the massive stars, i.e. that they would not have formed in the absence of the collision. Unfortunately, observational studies of this issue have an obvious drawback: they can only tell us what did happen, not what would have happened had the situation been different. Simulations, on the other hand, allow us to directly compare the outcome with or without a collision, or with different parameters for the collision, enabling us to better understand the extent to which the collision actually triggers star formation.

In the work presented here, we have insufficient dynamical range to follow the formation of individual stars, and so we cannot directly address the question of whether the collision makes massive star formation more likely. However, we can explore the more general question of whether star formation overall is triggered by the collision between our simulated clouds. Here, the lesson of the simulations is somewhat mixed. It is clear from the fact that star formation occurs in

our $v_{\rm rel} = 0\,{\rm km\,s^{-1}}$ control run that the cloud collision is not required in order for the clouds to begin forming stars, i.e. the collision does not trigger star formation in the sense that the clouds would otherwise remain starless. That said, the fact that star formation begins earlier in the colliding clouds and proceeds at a slightly higher rate are both indicative of the collision having a positive effect overall on the star formation efficiency of the cloud. It is possible that this enhancement of star formation would eventually be lost if we were to simulate the clouds for a much longer period. Conversely, it is also possible that the difference in efficiency would persist, particularly if the cloud lifetime is short. Ultimately, resolving this will require simulations that follow the evolution of the clouds for much longer periods that cover the long-scale collapse of the cloud, beyond the initial collision, and that also accounts for the stellar feedback processes responsible for dispersing them. However, this is outside of the scope of our current study.

5 CONCLUSIONS

In this paper, we presented the results of a series of simulations of the collision of two magnetized molecular clouds with mean hydrogen nuclei number densities $n \sim 80\,{\rm cm^{-3}}$ embedded in a warm, diffuse intercloud medium. In our simulations, we varied the relative velocity of the clouds, the inclination of the magnetic field relative to the collision axis, and the level of Jeans refinement adopted, and investigated the impact that these variations have on the resulting SFR. We found that that the different conditions caused star formation to occur at different times but that once star formation had begun, the subsequent evolution of the SFR was very similar in all of the simulations. Colliding clouds appear to form stars at a faster rate than clouds that do not collide, suggestive of some degree of triggering of star formation, but the difference in the SFRs is around a factor of two to three, in line with the results reported by Tanvir & Dale (2020) but much smaller than the order of magnitude increase found by Wu et al. (2017).

We further investigated the virial parameter of regions of gas around potential minima in our simulations, and how these virial parameters depend on the collisional velocity between the clouds. We found that the virial parameters in the potential minima were higher for the higher collisonal velocities, especially in the high-density, post-shocked gas, with higher amounts of turbulence in the

dense gas. Although the higher collision velocity simulations are found to create more high-density gas, our analysis demonstrates that much of this gas is not gravitationally bound, which explains why the correlation between collision velocity and SFR is so weak.

DATA AVAILABILITY

The data underlying this article will be shared on reasonable request to the corresponding author.

REFERENCES

André P. et al., 2010, A&A, 518, L102
Anicich V. G., Huntress W. T. J., 1986, ApJS, 62, 553
Astropy Collaboration, 2013, A&A, 558, A33
Astropy Collaboration, 2018, AJ, 156, 123
Badnell N. R. et al., 2003, A&A, 406, 1151
Badnell N. R., 2006, ApJS, 167, 334
Balfour S. K., Whitworth A. P., Hubber D. A., Jaffa S. E., 2015, MNRAS, 453, 2471
Barlow S. E., 1984, PhD thesis, University of Colorado at Boulder
Bate M. R., Bonnell I. A., Price N. M., 1995, MNRAS, 277, 362
Bertelli Motta C., Clark P. C., Glover S. C. O., Klessen R. S., Pasquali A., 2016, MNRAS, 462, 4171
Blitz L., 1993, in Levy E. H., Lunine J. I., eds, Protostars and Planets III. Univ. Arizona Press, Tucson, AZ, p. 125
Boldyrev S., 2006, Phys. Rev. Lett., 96, 115002
Bruderer S., 2019, Astrophysics Source Code Library, record ascl:1905.027
Cabral B., Leedom L. C., 1993, in Proceedings of the 20th Annual Conference on Computer Graphics and Interactive Techniques. SIGGRAPH '93. Association for Computing Machinery, New York, NY, USA, p. 263
Carty D., Goddard A., Köhler S. P. K., Sims I. R., Smith I. W. M., 2006, J. Phys. Chem. A, 110, 3101
Chevance M. et al., 2020, MNRAS, 493, 2872

Chira R. A., Beuther H., Linz H., Schuller F., Walmsley C. M., Menten K. M., Bronfman L., 2013, A&A, 552, A40
Clark P. C., Glover S. C. O., Klessen R. S., 2012, MNRAS, 420, 745
Clark P. C., Glover S. C. O., Ragan S. E., Duarte-Cabral A., 2019, MNRAS, 486, 4622
Dame T. M., Hartmann D., Thaddeus P., 2001, ApJ, 547, 792
de Ruette N., Miller K. A., O'Connor A. P., Urbain X., Buzard C. F., Vissapragada S., Savin D. W., 2016, ApJ, 816, 31
Dedner A., Kemm F., Kröner D., Munz C.-D., Schnitzer T., Wesenberg M., 2002, J. Comput. Phys., 175, 645
Dobbs C. L., Burkert A., Pringle J. E., 2011, MNRAS, 413, 2935
Dobbs C. L., Liow K. Y., Rieder S., 2020, MNRAS, 496, L1
Dobbs C. L., Pringle J. E., Duarte-Cabral A., 2015, MNRAS, 446, 3608
Dobbs C. L., Wurster J., 2021, MNRAS, 502, 2285
Draine B. T., 1978, ApJS, 36, 595
Draine B. T., Bertoldi F., 1996, ApJ, 468, 269
Federrath C., 2015, MNRAS, 450, 4035
Federrath C., Banerjee R., Clark P. C., Klessen R. S., 2010, ApJ, 713, 269
Ferland G. J., Korista K. T., Verner D. A., Ferguson J. W., Kingdon J. B., Verner E. M., 1998, PASP, 110, 761
Ferland G. J., Peterson B. M., Horne K., Welsh W. F., Nahar S. N., 1992, ApJ, 387, 95
Fujita S. et al., 2021, PASJ, 73, S201
Fukui Y. et al., 1999, PASJ, 51, 745
Fukui Y. et al., 2019, ApJ, 886, 14
Fukui Y., Habe A., Inoue T., Enokiya R., Tachihara K., 2021, PASJ, 73, S1
Fukui Y., Tsuge K., Sano H., Bekki K., Yozin C., Tachihara K., Inoue T., 2017, PASJ, 69, L5
Geppert W. D. et al., 2005, J. Phys: Conf. Ser., 4, 26
Glassgold A. E., Langer W. D., 1974, ApJ, 193, 73
Glover S. C. O., Clark P. C., 2012, MNRAS, 421, 116
Glover S. C. O., Federrath C., Mac Low M. M., Klessen R. S., 2010, MNRAS, 404, 2
Glover S. C. O., Jappsen A. K., 2007, ApJ, 666, 1
Gong M., Ostriker E. C., Wolfire M. G., 2017, ApJ, 843, 38
Grisdale K., Agertz O., Romeo A. B., Renaud F., Read J. I., 2017, MNRAS, 466, 1093
Habe A., Ohta K., 1992, PASJ, 44, 203
Habing H. J., 1968, Bull. Astron. Inst. Netherlands, 19, 421
Haid S., Walch S., Seifried D., Wünsch R., Dinnbier F., Naab T., 2018, MNRAS, 478, 4799
Harris C. R. et al., 2020, Nature, 585, 357
Haworth T. J., Shima K., Tasker E. J., Fukui Y., Torii K., Dale J. E., Takahira K., Habe A., 2015, MNRAS, 454, 1634
Heays A. N., Bosman A. D., van Dishoeck E. F., 2017, A&A, 602, A105
Hollenbach D., McKee C. F., 1979, ApJS, 41, 555
Hu Y., Federrath C., Xu S., Mathew S. S., 2022, MNRAS, 513, 2100
Hummer D. G., Storey P. J., 1998, MNRAS, 297, 1073
Hunter J. D., 2007, Comput. Sci. Eng., 9, 90
Jacobs T. A., Giedt R. R., Cohen N., 1967, J. Chem. Phys., 47, 54
Janev R. K., Langer W. D., Evans K., 1987, Elementary Processes in Hydrogen–Helium Plasmas – Cross Sections and Reaction Rate Coefficients. Springer, Berlin, Germany
Jones G. H., Clark P. C., Glover S. C. O., Hacar A., 2021, preprint (arXiv: 2112.05543)
Karpas Z., Anicich V., Huntress W. T., 1979, J. Chem. Phys., 70, 2877
Kim J. K., Theard L. P., Huntress W. T. J., 1975, Chem. Phys. Lett., 32, 610
Kippenhahn R., Weigert A., Weiss A., 2013, Stellar Structure and Evolution. Springer, Berlin
Krumholz M. R., McKee C. F., 2005, ApJ, 630, 250
Lada C. J., Lombardi M., Alves J. F., 2010, ApJ, 724, 687
Lepp S., Shull J. M., 1983, ApJ, 270, 578
Leroy A. K. et al., 2021, ApJS, 257, 43
Linder F., Janev R. K., Botero J., 1995, in Janev R. K., ed., Atomic and Molecular Processes in Fusion Edge Plasmas. Plenum Press, New York, p. 397
Liow K. Y., Dobbs C. L., 2020, MNRAS, 499, 1099
Mac Low M. M., Shull J. M., 1986, ApJ, 302, 585

Martin P. G., Keogh W. J., Mandy M. E., 1998, ApJ, 499, 793

Martin P. G., Schwarz D. H., Mandy M. E., 1996, ApJ, 461, 265

Matthaeus W. H., Pouquet A., Mininni P. D., Dmitruk P., Breech B., 2008, Phys. Rev. Lett., 100, 085003

McCall B. J. et al., 2004, Phys. Rev. A, 70, 052716

McElroy D., Walsh C., Markwick A. J., Cordiner M. A., Smith K., Millar T. J., 2013, A&A, 550, A36

McKinnon R., Torrey P., Vogelsberger M., Hayward C. C., Marinacci F., 2017, MNRAS, 468, 1505

Mitchell G. F., 1984, ApJS, 54, 81

Motte F., Bontemps S., Louvet F., 2018, ARA&A, 56, 41

Nahar S. N., 2000, ApJS, 126, 537

Neelamkodan N., Tokuda K., Barman S., Kondo H., Sano H., Onishi T., 2021, ApJ, 908, L43

Nelson R. P., Langer W. D., 1999, ApJ, 524, 923

Osterbrock D. E., 1989, Astrophysics of Gaseous Nebulae and Active Galactic Nuclei. University Science Books, Mill Valley, CA, USA

Pakmor R., Springel V., 2013, MNRAS, 432, 176

Pequignot D., Aldrovandi S. M. V., 1986, A&A, 161, 169

Petuchowski S. J., Dwek E., Allen J. E. J., Nuth J. A. I., 1989, ApJ, 342, 406

Powell K. G., Roe P. L., Linde T. J., Gombosi T. I., De Zeeuw D. L., 1999, J. Comp. Phys., 154, 284

Prasad S. S., Huntress W. T. J., 1980, ApJS, 43, 1

Prole L. R., Clark P. C., Klessen R. S., Glover S. C. O., 2022, MNRAS, 510, 4019

Rahner D., Pellegrini E. W., Glover S. C. O., Klessen R. S., 2017, MNRAS, 470, 4453

Rahner D., Pellegrini E. W., Glover S. C. O., Klessen R. S., 2019, MNRAS, 483, 2547

Roman-Duval J., Jackson J. M., Heyer M., Rathborne J., Simon R., 2010, ApJ, 723, 492

Scoville N. Z., Sanders D. B., Clemens D. P., 1986, ApJ, 310, L77

Sembach K. R., Howk J. C., Ryans R. S. I., Keenan F. P., 2000, ApJ, 528, 310

Shapiro P. R., Kang H., 1987, ApJ, 318, 32

Shore S. N., 1981, ApJ, 249, 93

Skarbinski M. S., Jeffreson S. M. R., Goodman A. A., 2023, MNRAS, 519, 1887

Smith B. D. et al., 2017, MNRAS, 466, 2217

Soler J. D., Hennebelle P., 2017, A&A, 607, A2

Sormani M. C. et al., 2019, MNRAS, 488, 4663

Springel V., 2005, MNRAS, 364, 1105

Springel V., 2010, MNRAS, 401, 791

Stancil P. C., Lepp S., Dalgarno A., 1998, ApJ, 509, 1

Stancil P. C., Schultz D. R., Kimura M., Gu J. P., Hirsch G., Buenker R. J., 1999, A&AS, 140, 225

Takahira K., Tasker E. J., Habe A., 2014, ApJ, 792, 63

Tan J. C., Beltrán M. T., Caselli P., Fontani F., Fuente A., Krumholz M. R., McKee C. F., Stolte A., 2014, in Beuther H., Klessen R. S., Dullemond C. P., Henning T., eds, Protostars and Planets VI. Univ. Arizona Press, Tuscon, AZ, p. 149

Tanvir T. S., Dale J. E., 2020, MNRAS, 494, 246

Tasker E. J., Tan J. C., 2009, ApJ, 700, 358

Tokuda K. et al., 2019, ApJ, 886, 15

Trevisan C. S., Tennyson J., 2002, Plasma Phys. Control. Fusion, 44, 1263

Tsang W., Hampson R. F., 1986, J. Phys. Chem. Ref. Data, 15, 1087

van Dishoeck E. F., 1988, in Millar T. J., Williams D. A., eds, Vol. 146, Rate Coefficients in Astrochemistry. Kluwer, Dordrecht, p. 49

Vissapragada S., Buzard C. F., Miller K. A., O'Connor A. P., de Ruette N., Urbain X., Savin D. W., 2016, ApJ, 832, 31

Voronov G. S., 1997, At. Data Nucl. Data Tables, 65, 1

Wakelam V. et al., 2010, Space Sci. Rev., 156, 13

Wareing C. J., Pittard J. M., Falle S. A. E. G., 2017, MNRAS, 470, 2283

Weingartner J. C., Draine B. T., 2001, ApJ, 563, 842

Wolfire M. G., Tielens A. G. G. M., Hollenbach D., Kaufman M. J., 2008, ApJ, 680, 384

Wollenberg K. M. J., Glover S. C. O., Clark P. C., Klessen R. S., 2020, MNRAS, 494, 1871

Wu B., Tan J. C., Christie D., Nakamura F., Van Loo S., Collins D., 2017, ApJ, 841, 88

Wu B., Van Loo S., Tan J. C., Bruderer S., 2015, ApJ, 811, 56

Zanchet A., Bussery-Honvault B., Jorfi M., Honvault P., 2009, Phys. Chem. Chem. Phys. (Inc. Faraday Trans.), 11, 6182

APPENDIX A: CHEMICAL NETWORK

The reactions included in our chemical network are summarized in Tables A1 and A2. Our network is based on the one presented by Gong, Ostriker & Wolfire et al. (2017, hereafter 2017), but also

Table A1. List of collisional chemical reactions included in our chemical network.

No.	Reaction	Notes	Refs.
1	$H + e^- \rightarrow H^+ + e^- + e^-$		1
2	$H^+ + e \rightarrow H + \gamma$		2
3	$He^+ + H_2 \rightarrow H_2^+ + He$		3
4	$He^+ + H_2 \rightarrow H^+ + H + He$		3
5	$H_2 + e^- \rightarrow H + H + e^-$	Not in 2017	4
6	$H_2 + H \rightarrow H + H + H$	Different rate	5, 6, 7
7	$H_2 + H_2 \rightarrow H + H + H_2$	Different rate	8, 9
8	$H_2^+ + H_2 \rightarrow H_3^+ + H$	Different rate	10
9	$H_2^+ + H \rightarrow H_2 + H^+$		11
10	$H_3^+ + e^- \rightarrow H + H + H$		12
11	$H_3^+ + e^- \rightarrow H_2 + H$		12
12	$He + e^- \rightarrow He^+ + e^- + e^-$	Not in 2017	1
13	$He^+ + e^- \rightarrow He + \gamma$	Different rate	13, 14
14	$C^+ + H_2 \rightarrow CH_x + H$		15, 16
15	$C^+ + H_2 + e^- \rightarrow C + H + H$		15, 16
16	$C + H_2 \rightarrow CH_x + \gamma$	Not in 2017	17
17	$C + H_3^+ \rightarrow CH_x + H_2$		18
18	$C^+ + e^- \rightarrow C + \gamma$	Different rate	14, 19
19	$C + e^- \rightarrow C^+ + e^- + e^-$	Not in 2017	20
20	$O^+ + H \rightarrow O + H^+$		21
21	$O + H^+ \rightarrow O^+ + H$		21
22	$O^+ + H_2 \rightarrow OH_x + H$		16
23	$O^+ + H_2 + e \rightarrow O + H + H$		16
24	$O + H_3^+ \rightarrow OH_x + H_2$		22
25	$O + H_3^+ + e^- \rightarrow H_2 + O + H$		22
26	$C^+ + OH_x \rightarrow HCO^+$		16
27	$C + OH_x \rightarrow CO + H$		23
28	$CH_x + He^+ \rightarrow C^+ + He + H$	Not in 2017	17, 24
29	$CH_x + H \rightarrow H_2 + C$		15
30	$CH_x + O \rightarrow CO + H$		15
31	$OH_x + H \rightarrow O + H_2$	Not in 2017	24, 25
32	$OH_x + O \rightarrow O + O + H$		26
33	$OH_x + He^+ \rightarrow O^+ + He + H$		15
34	$CO + H_3^+ \rightarrow HCO^+ + H_2$		27
35	$CO + He^+ \rightarrow C^+ + O + He$	Different rate	28
36	$CO + H \rightarrow C + OH_x$	Not in 2017	29
37	$HCO^+ + e^- \rightarrow OH_x + C$	Not in 2017	30
38	$HCO^+ + e^- \rightarrow CO + H$		30
39	$Si^+ + e^- \rightarrow Si + \gamma$	Different rate	31
40	$Si + e^- \rightarrow Si^+ + e^- + e^-$	Not in 2017	20

References: 1: Janev, Langer & Evans (1987); 2: Ferland et al. (1992); 3: Barlow (1984); 4: Trevisan & Tennyson (2002); 5: Mac Low & Shull (1986); 6: Lepp & Shull (1983); 7: Martin, Schwarz & Mandy (1996); 8: Martin, Keogh & Mandy (1998); 9: Jacobs, Giedt & Cohen (1967); 10: Linder, Janev & Botero (1995); 11: Karpas, Anicich & Huntress (1979); 12: McCall et al. (2004); 13: Hummer & Storey (1998); 14: Badnell (2006); 15: Wakelam et al. (2010); 16: Gong et al. (2017); 17: Prasad & Huntress (1980); 18: Vissapragada et al. (2016); 19: Badnell et al. (2003); 20: Voronov (1997); 21: Stancil et al. (1999); 22: Fit by 2017 to de Ruette et al. (2016); 23: Zanchet et al. (2009); 24: McElroy et al. (2013) 25: Tsang & Hampson (1986); 26: Carty et al. (2006); 27: Kim, Theard & Huntress (1975); 28: Petuchowski et al. (1989); 29: Mitchell (1984); 30: Geppert et al. (2005); 31: Nahar (2000).

Table A2. List of grain surface, cosmic ray, and photochemical reactions included in our chemical network.

No.	Reaction	Notes	Refs.
41	$H + H + gr \rightarrow H_2 + gr$	Different rate	1
42	$H^+ + e^- + gr \rightarrow H + gr$	Different rate	2
43	$C^+ + e^- + gr \rightarrow C + gr$	Different rate	2
44	$He^+ + e^- + gr \rightarrow He + gr$	Different rate	2
45	$Si^+ + e^- + gr \rightarrow Si + gr$	Different rate	2
46	$H + cr \rightarrow H^+ + e^-$		3
47	$H_2 + cr \rightarrow H_2^+ + e^-$		3
48	$H_2 + cr \rightarrow H + H^+ + e^-$	Not in 2017	4
49	$H_2 + cr \rightarrow H + H$	Not in 2017	4
50	$He + cr \rightarrow He^+ + e^-$		4
51	$C + cr \rightarrow C^+ + e^-$		4
52	$CO + cr + H \rightarrow HCO^+ + e^-$		5
53	$C + \gamma_{cr} \rightarrow C^+ + e^-$		6
54	$CO + \gamma_{cr} \rightarrow C^+ + e^-$		6
55	$Si + \gamma_{cr} \rightarrow Si^+ + e^-$		6
56	$C + \gamma \rightarrow C^+ + e^-$		6
57	$CH_x + \gamma \rightarrow C + H$		5,6
58	$CO + \gamma \rightarrow C + O$		6
59	$OH_x + \gamma \rightarrow O + H$		5,6
60	$Si + \gamma \rightarrow Si^+ + e^-$		7
61	$H_2 + \gamma \rightarrow H + H$		8

Note. The primary cosmic ray ionization rate of atomic hydrogen is a free parameter in our chemical model and the value we select for this in our simulations is discussed in the main text. The total (primary plus secondary) rate for H (reaction 46), as well as the total cosmic ray ionization rates of H_2, He, C, CO, and Si (reactions 47–55), are scaled relative to this value using scaling factors derived from the cited references.
References: 1: Hollenbach & McKee (1979); 2: Weingartner & Draine (2001), modified as described in the text; 3: Glassgold & Langer (1974); 4: McElroy et al. (2013); 5: Gong et al. (2017); 6: Heays, Bosman & van Dishoeck (2017); 7: van Dishoeck (1988); 8: Draine & Bertoldi (1996).

includes several reactions not included in their network, denoted in the tables as 'Not in 2017'. In addition, for some reactions, we have adopted a different rate coefficient from the one listed in 2017; these are also indicated in the Table, with the note 'Different rate'. Reactions with no attached note are treated exactly the same as in 2017. Below, we discuss the rationale for the differences between our network and the original 2017 network. For the most part, these differences are to make the network more robust when applied to physical conditions outside of the range considered by 2017 and have little impact on its behaviour in the typical PDR conditions that were the main focus of their study.

Reactions in our network that are not in 2017

Reactions 5, 12, 19, & 40

These reactions – the collisional dissociation of H_2 by electrons and the collisional ionization of He, C, and Si – were neglected by 2017 because they are unimportant at typical PDR temperatures. However, they can become important in hot shocked gas with $T \gg 10^4$ K, and we include them to ensure that the chemical network behaves reasonably at these high temperatures.
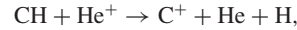
Reaction 16

The formation of CH_x – a pseudo-molecule that represents light hydrocarbons such as CH, CH_2, CH^+ etc. – by radiative association of atomic carbon and H_2 is neglected by 2017 because it is a slow process and in typical Milky Way conditions is unimportant

compared to CH_x formation via the reaction of C and H_3^+ (reaction 17). However, the abundance of H_3^+, and hence the rate of reaction 17, depends sensitively on the cosmic ray ionization rate, and so reaction 16 can become important in conditions where this is much smaller than the typical Milky Way value.
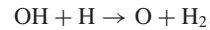
Reaction 28

In neutral gas, this reaction is unimportant compared to reaction 29. It is included here to ensure that an appropriate loss route exists for CH_x in very highly ionized gas. For the rate coefficient, we use the value given by McElroy et al. (2013) for the reaction

$$CH + He^+ \rightarrow C^+ + He + H,$$

which comes originally from Prasad & Huntress (1980).

Reaction 31

This reaction is unimportant compared to reaction 32 at temperatures lower than 500 K, but quickly becomes dominant at higher temperatures, given a sufficient supply of hydrogen atoms. It is therefore not important in typical PDR conditions but can become important in shocks. For the rate coefficient, we adopt the value given by McElroy et al. (2013) for the reaction

$$OH + H \rightarrow O + H_2,$$

which is based on Tsang & Hampson (1986).

Reaction 36

This reaction has a substantial activation energy ($E/k \sim 78\,000$ K) and is therefore unimportant in typical PDR conditions. However, it can become important in hot, shocked gas. In particular, we have found that if strong shocks occur in gas with high A_V, CO can persist in the gas up to artificially high temperatures of $> 10^4$ K if this reaction is not included.

Reaction 37

As 2017 note in their appendix A, the destruction of HCO^+ is dominated by the reaction $HCO^+ + e^- \rightarrow CO + H$ (reaction 38 above). However, although CO and H are the most likely products of the dissociative recombination of HCO^+, roughly 8 per cent of the time this process instead yields C and OH (Geppert et al. 2005). We include this outcome here for completeness.

Reactions 48 & 49

Although interactions between high energy cosmic rays and H_2 molecules primarily produce H_2^+ ions (reaction 47), a small fraction of the time the outcome can instead be a hydrogen atom, a proton, and an electron (reaction 48) or two hydrogen atoms (reaction 49). These outcomes were neglected by 2017 but we include them here for completeness.

Reactions with different rate coefficients

Reactions 6 & 7

We use the same low-density limits for the rates of these reactions as in 2017, and the same expression for the H_2 critical density. However,

we use slightly different expressions for the high-density limits: 2017 follow Lepp & Shull (1983) and Shapiro & Kang (1987) for reactions 6 and 7, respectively, whereas we use the expression given by Martin et al. (1996) for the high-density limit of reaction 6 and adopt a value eight times smaller than this for reaction 7, following Jacobs et al. (1967). At densities below the H_2 critical density ($n \sim 10^4 \, \mathrm{cm}^{-3}$), we therefore recover the same behaviour as in 2017, and we also find good agreement between the different treatments in hot ($T > 6000 \, \mathrm{K}$), high-density gas. The only significant difference comes in cool dense gas, where the Lepp & Shull (1983) expression overestimates the H_2 collisional dissociation rate. However, given the small size of this rate at these temperatures, this difference is likely only of minor importance.

Reaction 8

We adopt the rate coefficient for this reaction given in Stancil, Lepp & Dalgarno (1998), which is their fit to cross-section data from Linder et al. (1995). 2017 also cite Linder et al. (1995) as the source of their rate coefficient, but their expression is $\sim$27 per cent larger than the one given in Stancil et al. (1998). The source of this discrepancy is unclear. However, in practice, it is unlikely to be important as this reaction is never the rate-limiting step for the formation of H_3^+.

Reaction 13

2017 assume case B for the radiative recombination of He^+ and use a reaction rate coefficient from Glover et al. (2010) that is a fit to the values tabulated by Hummer & Storey (1998). Our treatment differs from this in two respects. First, in addition to radiative recombination, we also account for dielectronic recombination of He^+, using a rate coefficient from Badnell (2006). Secondly, although we assume the on-the-spot approximation applies, we do not assume pure case B recombination for He^+, which would be valid only in a gas consisting of pure helium. Instead, we follow Osterbrock (1989) and account for the fact that some of the photons produced during the recombination of He^+ are absorbed by atomic hydrogen rather than He. (A more detailed discussion of how this is done can be found in Glover & Jappsen 2007).

Reaction 18

As in 2017, we adopt a rate coefficient for C^+ recombination that is the sum of two contributions: one corresponding to radiative recombination, taken from Badnell (2006), and one corresponding to dielectronic recombination, taken from Badnell et al. (2003). In the expression that they use for the dielectronic recombination rate, 2017 retain only the first three terms, which is sufficient at low temperatures but which leads to inaccuracies at high temperatures ($T \gg 10^4 \, \mathrm{K}$). In our implementation of this rate, we instead retain all of the terms from the expression given by Badnell et al. (2003).

Reaction 35

2017 adopt a temperature-independent rate for this reaction from Anicich & Huntress (1986), whereas we adopt the temperature-dependent value proposed by Petuchowski et al. (1989). In practice, there is very little difference between these two values at typical PDR temperatures.

Reaction 39

2017 adopt a rate coefficient for this reaction that they credit to McElroy et al. (2013) but that derives originally from Pequignot & Aldrovandi (1986). However, this fit is formally valid only in the temperature range $10 < T < 1000 \, \mathrm{K}$. Moreover, it only accounts for the contribution from radiative recombination, and not the dielectronic recombination term that dominates at high temperatures. We adopt instead a rate from Nahar (2000) that accounts for both processes.

Reaction 41

2017 adopt a constant value of $3 \times 10^{-17} \, \mathrm{cm}^3 \, \mathrm{s}^{-1}$ for the rate coefficient for this reaction. We instead adopt the rate coefficient given in Hollenbach & McKee (1979), which depends on the temperatures of both the gas and the dust grains.

Reaction 42–45

We follow 2017 in which we use the reaction rate coefficients given in Weingartner & Draine (2001) for the recombination of H^+, C^+, He^+, and Si^+ ions on grain surfaces (reactions 42–45), multiplied by a factor of 0.6 to better match the results of Wolfire et al. (2008). These rate coefficients depend primarily on the parameter

$$\psi = \frac{G\sqrt{T}}{n_e}, \tag{A1}$$

where G is the local value of the ISRF in Habing (1968) units and n_e is the electron number density. One important way in which our treatment differs from 2017 is in our treatment of these rate coefficients for low values of ψ. The expressions given in Weingartner & Draine (2001) are stated to be valid only for $\psi > 100 \, \mathrm{K}^{1/2} \, \mathrm{cm}^3$ and applying them unaltered when the value of ψ is smaller than this yields recombination rates that are significant overestimates of the true values. To avoid this, we simply assume that the rates in gas with $\psi < 100 \, \mathrm{K}^{1/2} \, \mathrm{cm}^3$ are the same as those in gas with $\psi = 100 \, \mathrm{K}^{1/2} \, \mathrm{cm}^3$ (cf. fig. 3 of Weingartner & Draine 2001).

The other main difference between our treatment and that in 2017 is that we multiply the grain surface recombination rates by an additional factor of $\exp(-T/34\,000)$. This is to ensure that the recombination rates fall rapidly to zero in very hot gas, in conditions where we expect that in reality the dust would be quickly destroyed by sputtering. This modification would not be necessary if we were using a more sophisticated treatment of dust evolution that accounted for this effect (see e.g. McKinnon et al. 2017), but this is a topic for future work.

APPENDIX B: POST-COLLISION MAGNETIC FIELD

Here, we illustrate how the magnetic field is warped in the process of the collision of the clouds. Figs B1 and B2 show images of the magnitude and z-component of the magnetic field, respectively, which have been convolved with the x-y components of magnetic field via line integral convolution (LIC; Cabral & Leedom 1993). This is done to give indication of the direction of the magnetic field in the x-y plane.

We noted in Section 3.1 that an early onset of star formation is observed for a magnetic field inclination of $\theta = 0$, i.e. a field that is initially parallel to the collision axis. In this case, the magnetic field is not compressed during the collision and hence does not hinder the collision process. This can be seen clearly in the central panels
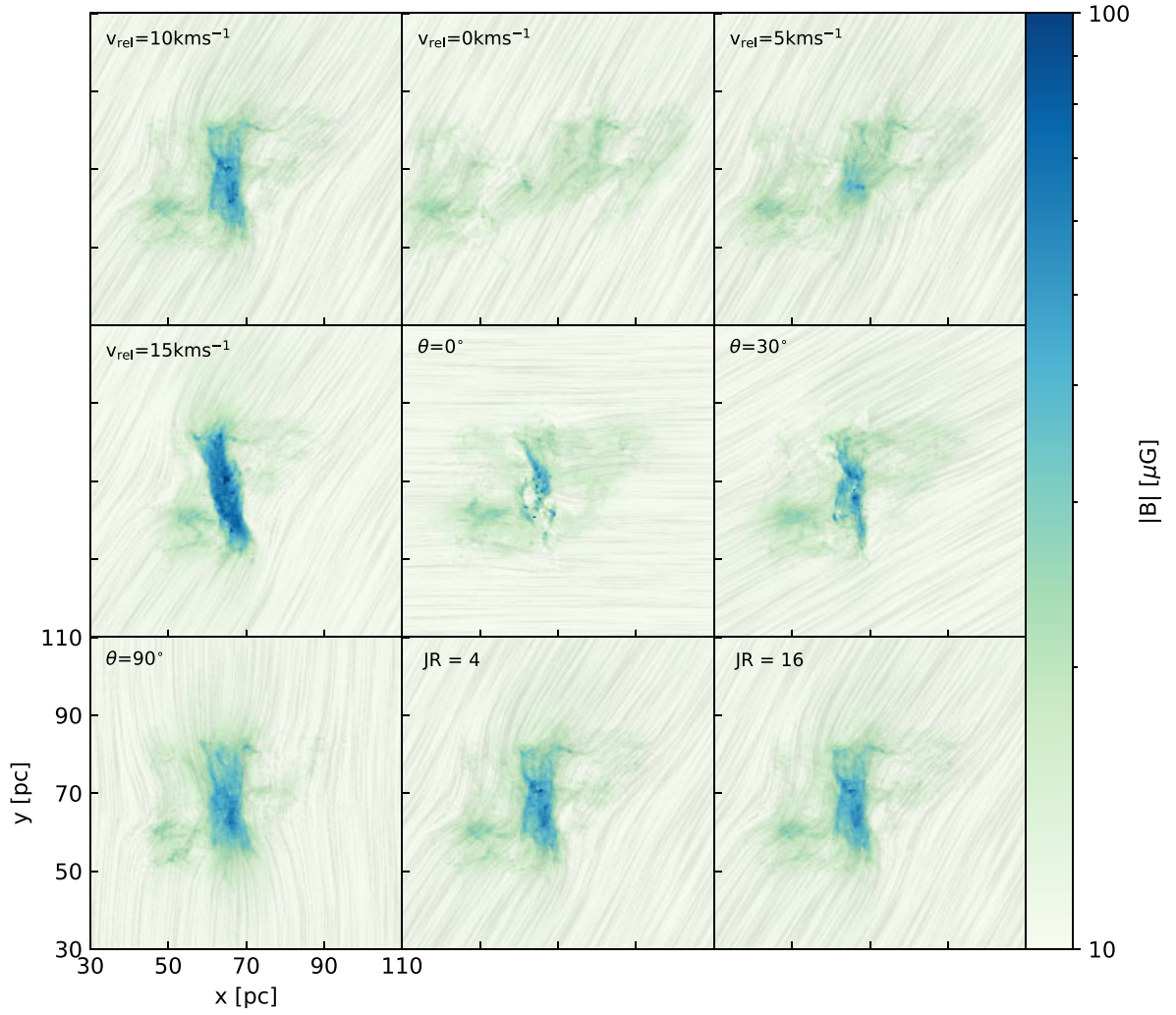
Figure B1. Maps of the magnetic field strength of the simulations carried out at $t = 2.40$ Myr. LIC is used on the map to indicate the direction of the magnetic field in the x–y plane.

of Figs B1 and B2, where the pattern of the map generated by the LIC lies predominantly parallel to the x-axis. Only at the site of the collision is the magnetic field distorted, owing to the local collapse of the gas.
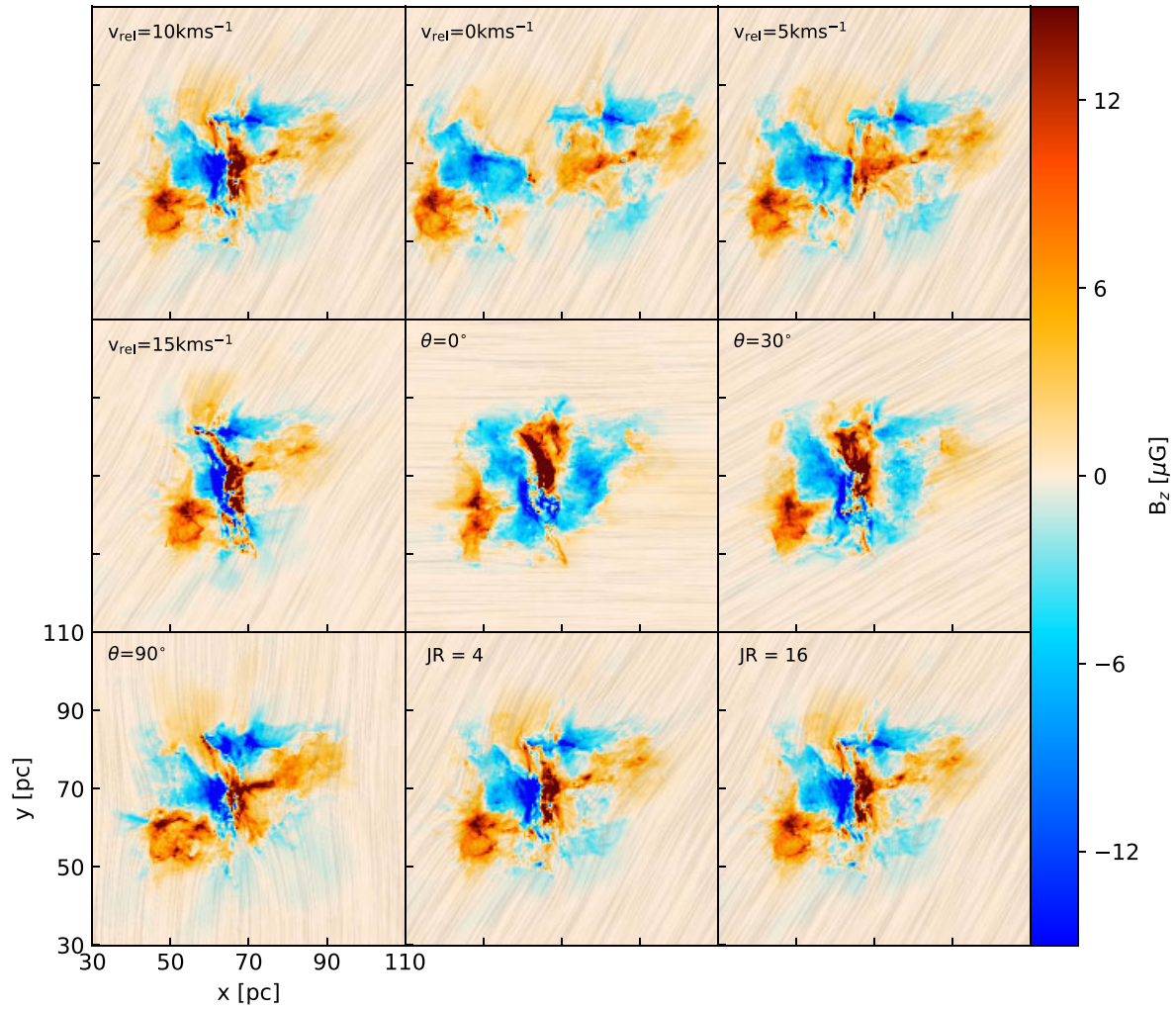
Figure B2. Same as Fig. B1 but for the z component of the magnetic field.

This paper has been typeset from a TEX/LATEX file prepared by the author.